LITHOS 508–509 (2025) 108106

Contents lists available at ScienceDirect

LITHOS

journal homepage: www.elsevier.com/locate/lithos

Triassic lamprophyre dyke in the Palaeozoic basement of NE Sardinia, Italy: Petrogenesis and geodynamic significance

Gabriele Cruciani [a,*], Dario Fancello [a], Mattia Ferrari [b], Alessandro Bragagni [b,c], Simone Tommasini [b,d], Marcello Franceschelli [a]

[a] Dipartimento di Scienze Chimiche e Geologiche, Università degli Studi di Cagliari – S.S. 554 Cittadella Universitaria, 09042 Monserrato, CA, Italy
[b] Dipartimento di Scienze della Terra, Università degli Studi di Firenze, via La Pira 4, 50121 Firenze, Italy
[c] C.N.R., Institute of Marine Sciences, 40129, via G. Gobetti 101, Bologna, Italy
[d] C.N.R., Institute of Geosciences and Georesources, via La Pira 4, 50121 Firenze, Italy

ARTICLE INFO

Keywords:
Lamprophyre
Geochemical and radiogenic isotope signature
Geodynamic setting
Pangea breakup
Sardinia

ABSTRACT

A Triassic, Si-undersaturated, alkaline lamprophyre from NE Sardinia is studied to decipher its magma source, genesis, and P-T conditions of crystallization and emplacement. It is also compared with similar and coeval rocks occurring throughout Europe to depict a geodynamic scenario associated with the opening of the Pangea. The lamprophyre, crosscutting the Palaeozoic basement, shows a porphyritic texture with centimeter-sized amphibole macrocrystals and biotite, ulvöspinel and apatite phenocrystals. The lamprophyre also contains feldspar clusters, carbonate-rich inclusions, and xenolith nodules. The incompatible trace element patterns show weak positive anomalies for Ba, Nb, K and P and negative ones for Th and Ta, whereas the chondrite-normalized Rare Earth Elements (REE) pattern reflects a constant fractionation from light REEs to heavy REEs without Eu anomaly. The core of the amphibole reflects the deepest crystallization conditions, whereas rims and groundmass amphiboles indicate slightly higher temperature and lower pressure. The bulk Sr and Nd radiogenic isotope composition falls between the *E*-DMM and BSE mantle components at 220 Ma, ruling out a significant contribution of the local lithospheric mantle, which was metasomatized during the Hercynian orogeny. The comparison with other European lamprophyres along with a palaeogeographic reconstruction suggests that the Sardinia lamprophyre lies along the eastern branch of the fault system responsible for to the opening of the Alpine Tethys. The trace element and radiogenic isotope signature of the Sardinian and the other European lamprophyres is consistent with a progressive transition from the post-collisional orogenic magmatism to anorogenic rift-related alkaline magmatism occurring during Early Mesozoic break-up of Pangea and opening of the Tethys Ocean.

1. Introduction

During the Permo-Triassic, widespread magmatic activity occurred across a broad area of the European continent, from present-day Alpine Corsica to the Southern Alps and Dinarides (Castellarin et al., 1988; De Min et al., 2020; Pamić, 1984). This activity is thought to be related to extensional and strike-slip tectonics associated with the subduction of the Palaeotethys Ocean.

The emplacement of lamprophyric dykes, in this framework, characterized several plutonic complexes in southern Europe, providing relevant information on the geodynamic setting (Casetta et al., 2019). Lamprophyres are thought to form by partial melting of a metasomatized mantle (Pandey et al., 2017a, 2017b; Rock, 1991; Soder and Romer, 2018; Stoppa et al., 2014) and their emplacement is commonly attributed to the beginning of lithospheric extensional–-transtensional tectonics. Alkaline lamprophyres, derived from the Earth mantle at depths of 100–150 km (e.g., Bédard, 1994; Bernard-Griffiths et al., 1991), can contain carbonate ocelli, suggesting the presence of CO_2 in their mantle source. Their study can help to elucidate the role of CO_2–H_2O-rich fluids during mantle metasomatism (Bouabdli et al., 1988; Hidas et al., 2010).

These rocks are also important since their occurrence in the geological record of an area may mark transition between different geodynamic regimes and tectonic settings (Scarrow et al., 2011).

* Corresponding author.
E-mail address: gcrucian@unica.it (G. Cruciani).

https://doi.org/10.1016/j.lithos.2025.108106
Received 18 September 2024; Received in revised form 17 April 2025; Accepted 18 April 2025
Available online 24 April 2025

Calcalkaline lamprophyres are found in convergent settings, whereas alkaline varieties are associated to divergent margins and continental intra-plate settings (Batki et al., 2014; Lu et al., 2015; Pandey et al., 2017a, 2017b; Rock, 1991; Stoppa et al., 2014; Ubide et al., 2014). In particular, alkaline lamprophyres are widely recognized at divergent margins (rift valleys, triple junctions) and in intra-plate (oceanic islands, hot-spots) tectonic settings, being genetically associated with alkali basaltic magmatism (e.g., Orejana et al., 2008; Tappe et al., 2006).

A mantle plume connection for alkaline lamprophyres of the Permian Tarim Large Igneous Province has been suggested by Liu et al. (2023). In the Bohemian Massif, Krmíček et al. (2020) documented the evolution from a Carboniferous orogenic lamprophyre-lamproite association to a Permian anorogenic lamprophyre association.

In NE Sardinia, in proximity of Fr.cu E M. Nieddu (FMN), near Lodé, Baldelli et al. (1987) first described an undeformed Permo-Triassic alkaline lamprophyre dyke, characterized by centimetric biotite and amphibole euhedral crystals, and classified as camptonite by these authors. The dyke intruded the micaschists of the Variscan metamorphic basement of NE Sardinia and represents the only known occurrence of alkaline lamprophyre in Sardinia.

In this manuscript, we present and discuss mineral chemistry data, whole rock major and trace elements, and Sr—Nd radiogenic isotope compositions of the FMN lamprophyre with the following aims: (i) to provide a petrological and geochemical characterization; (ii) to define the nature of the mantle sources; and (iii) to improve the knowledge of the tectonic setting and significance of the alkaline lamprophyre.

The study of this Triassic lamprophyre dyke that was fully preserved from the Alpine overprint is also relevant for deciphering its connection with the host metamorphic basement as well as for understanding the post-magmatic evolution of the Sardinia-Corsica microplate. It is worth noting that the Sardinian-Corsican block, up to the early Cenozoic, was attached to Variscan France (Provence) and only after the Oligo-Miocene rotation reached the current geographic position in the western Mediterranean. Therefore, the FMN lamprophyre could help to constrain the palaeogeographic position of the Sardinian block during the Trias. The collected data will be compared with those from similar rocks in neighbouring terranes in Europe and will be interpreted in the framework of their relationships with other magmatic occurrences. A palaeogeographic reconstruction of alkaline lamprophyre occurrences at the onset of the opening of the Tethyan Ocean will be also presented.

2. Geological framework

The Sardinia-Corsica microplate is located in the centre of the western Mediterranean Sea. During the Cenozoic, this microplate was separated from the European palaeo-continent by rifting and continental drift with counterclockwise translation and rotation towards its current position (Alvarez, 1972).

The Sardinia basement was affected by Variscan deformation and metamorphism resulting in a S to SW-verging stacking of tectonic units

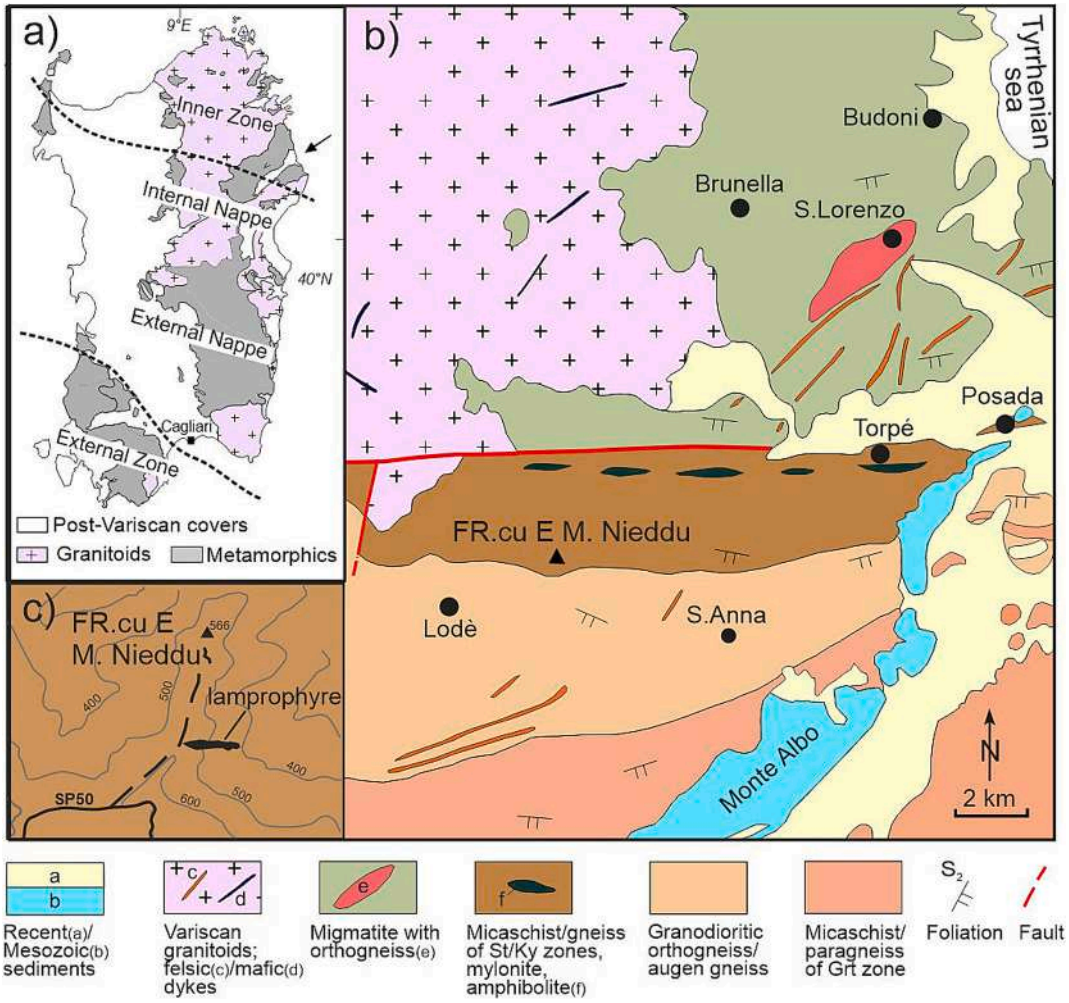

Fig. 1. a) Tectonic sketch map of the Variscan chain of Sardinia (the arrow refers to the study area shown in b) and c); b) Simplified geological map of NE Sardinia Palaeozoic basement modified after Cruciani et al. (2022) and references therein. The FR.cu E M. Nieddu sample locality (40°36′14″N, 9°35′10″E) is also shown. St: staurolite; Ky: kyanite; Grt: garnet; c) Map of the Fr.cu E M. Nieddu lamprophyre; not to scale.

with increasing metamorphic grade from SW to NE. From south to north, the metamorphic basement consists of the following three main tectono-metamorphic zones (Carmignani et al., 2001): External Zone, Nappe Zone and Inner Zone (Fig. 1a) that continues in southern Corsica (Cruciani et al., 2021; Rossi et al., 2009). The inner zone is characterized by pelitic metasedimentary sequences up to migmatite (Fancello et al., 2018) with retrogressed eclogite and granulite facies rocks (Scodina et al., 2019).

In northern Sardinia, a regional scale transpressive shear zone known as the Posada-Asinara Shear Zone (PASZ, Carosi et al., 2020; Fig. 1a) separates the Medium-Grade Metamorphic Complex (MGMC) to the south from the High-Grade Metamorphic Complex (HGMC, also known as Migmatite Complex) to the north.

The basement is extensively intruded by the igneous rocks of the Sardinia-Corsica batholith, dated in Sardinia from ca. 320 to 285 Ma and in Corsica from ca. 336 to 284 Ma (Casini et al., 2012). These igneous and metamorphic rocks of the Palaeozoic basement are covered by volcanic and sedimentary rocks laying on intra-continental sedimentary basins of late Carboniferous-Permian age, followed by Mesozoic carbonate rocks (Carmignani et al., 2001). The late Carboniferous to lower Permian volcanism includes a variety of intermediate to silicic products with medium- to high-K calc-alkaline andesites, dacites, and rhyolites outcropping in the north and central Sardinia continental basins (Cortesogno et al., 1998; Gaggero et al., 2017; Traversa et al., 2003).

Igneous zircons from calc-alkaline silicic volcanic rocks yield ages between 299 ± 1 and 288 ± 3 Ma, whereas andesites emplaced in medium-grade metamorphic basement of south-central Sardinia (Ogliastra) show a cluster of older ages at 332 ± 12 Ma (Gaggero et al., 2017).

Dyke swarms crosscut both the Variscan metamorphic basement and the Permian volcanic units (Traversa et al., 1997, 2003). In Sardinia and Corsica, the dyke activity developed in two main phases: from the Late Carboniferous to Upper Permian, and from the Late Permian to Upper Triassic(?) (Vaccaro et al., 1991). The former dyke intrusions (Late Carboniferous–Upper Permian) reflect an orogenic environment, and are medium- high-K calc-alkaline basaltic andesites up to rhyolites and peraluminous rhyolites. The latter dyke intrusions consist of transitional basalts with minor tholeiitic and alkaline basalts.

2.1. The lamprophyre dyke

The FMN lamprophyre, partially covered by bushes and vegetation at the top of a small hill (Fig. 2a), is an undeformed mafic dyke exposed along a country road in the forest north of the SP50 road, which connects S. Anna with Lodé villages in NE Sardinia (Fig. 1b). The outcrop is located near the boundary between the Medium Grade Metamorphic Complex and the High Grade Metamorphic Complex, in the south-eastern sector of the Posada-Asinara Shear Zone. South of the study area, granodioritic orthogneiss and augen gneiss—part of the so called Lodé-Mamone antiform—are exposed, whereas amphibolite lenses, embedded within the metasedimentary sequence, are aligned along the Posada-Asinara Shear Zone, northwards from the studied camptonite.

The dyke, which crosscuts the micaschists of the staurolite + kyanite zone, is 2–3 m wide and approximately 100–150 m long, is oriented N40° and shows a discordant contact with respect to the main direction of regional schistosity of the surrounding metamorphic rocks (Fig. 2b). It

Fig. 2. a) Lamprophyre location (arrow) at Fr.cu E M. Nieddu area; b) Field appearance of the lamprophyre dyke intruding the micaschist in the staurolite/kyanite zone; c) Centimetric amphibole and biotite in the greyish fine-grained groundmass of the lamprophyre dyke; d) Greenish xenolith nodule in a hand sample. Mineral abbreviations from Whitney and Evans (2010).

is easily distinguished by its dark-green colour and isotropic texture that strongly contrasts with the brownish colour and schistose appearance of the host rocks. Contacts with the surrounding host rocks are generally sharp, and no significant thermometamorphic evidence is observed. Abundant and coarse-grained (up to 3 cm in size) biotite and amphibole, nearly idiomorphic and homogeneously distributed into a greyish fine-grained groundmass, are visible at the hand-specimen and outcrop scale (Fig. 2c). Several centimetric to millimetric greenish xenolith nodules are also observed with the naked eye (Fig. 2d). The FMN lamprophyre has been classified as a camptonite of basanitic composition (Baldelli et al., 1987), based upon mineral paragenesis, and major and trace element data. Successively, Gaggero et al. (2007) classified the lamprophyre has a tephrite with an alkali-basalt composition (Nb/Y-Zr/TiO_2 diagram, Winchester and Floyd, 1977).

Baldelli et al. (1987) reported amphibole and biotite K—Ar age of 227.6 ± 3 Ma and 214.5 ± 10.7 Ma, respectively. Fission track dating provided ages of 229 ± 10 Ma, 240 ± 11 Ma, 235 ± 13 Ma, 227 ± 15 Ma on apatite, and 245 ± 20 Ma, 247 ± 20 Ma, 224 ± 16 Ma on biotite (Baldelli et al., 1987).

For a more detailed structural reconstruction of the relationships between the metasedimentary sequences, granodioritic orthogneiss and augen gneiss exposed in the study area, the reader is referred to Cruciani et al. (2015, 2022) and Carosi et al. (2020).

3. Analytical methods

Twenty thin sections of the lamprophyre dyke were prepared for petrographic investigation. The most representative thin sections were polished and carbon-coated for detailed microstructural study using a FEI Quanta 200 SEM equipped with a nitrogen-free Thermofisher™ UltraDry EDS Detector installed at Centro Servizi d'Ateneo per la Ricerca (CeSAR), Università di Cagliari. Quantitative chemical analyses of amphibole, biotite, feldspar, and other silicate minerals were performed with a CAMECA SX100 electron microprobe (EMP) equipped with five wavelength-dispersive spectrometers installed at the Institut für Anorganische Chemie, Universität Stuttgart. Synthetic and natural minerals, glasses and pure oxides were used as standards. The acceleration voltage, beam current and beam diameter were 15 kV, 15 nA, and 5 μm, respectively. The PaP correction procedure provided by CAMECA was applied.

X-ray concentration maps for amphibole were obtained by stepwise scanning of the thin sections under the EMP beam, with a 100 ms counting time per step and an electric current of 50 nA. Trace elements (Sc, Rb, Sr, Y, Nb, Ba, Hf, Ta, Th, V, Cr, Zr, U) and rare earth element (REE) abundances in selected amphibole and biotite crystals were acquired at Cagliari University with a Quadrupole ICP-MS Perkin Elmer Elan DRC-e coupled with a 213 nm Nd:YAG New Wave Research laser. Measurements were made with 46–50 mJ laser energy, 40–100 μm spot sizes, 0.2 mJ pulse energy, 10 hz frequency, 50–60 s ablation time, 60 s background, and 30 s washout delay. Analyses were calibrated against the silicate glass reference material NIST SRM 612 and the glass BCR-2G was measured as an unknown to monitor accuracy. Data reduction was made with Glitter using ^{29}Si as internal standard, using concentrations determined by EMP.

Nine samples from the dyke were then analyzed for bulk rock major and trace elements at the ALS Minerals Laboratories, Seville, Spain, using X-ray fluorescence and ICP-MS spectrometry, respectively.

Carbon content was measured with a CHNS/O micro analyzer Perkin Elmer2400 series II after lithium tetraborate fusion and four acids digestion. Acetanilide (C = 71.09 wt%; H = 6.71 wt%; N = 10.36 wt%) was used as calibration standard. Sr and Nd isotopes were analyzed at the Department of Earth Sciences, Università degli Studi di Firenze. Sample powders (20 mg) were dissolved in a HF–HNO_3–HCl mixture. Sr and Nd fractions were separated following standard chromatographic techniques using AG50x8 and PTFE–HDEHP resins with HCl as eluent. The total procedural blank was <200 pg for Sr and < 100 pg for Nd, making blank correction negligible. Isotope measurements were performed on a ThermoFisher Triton-Ti thermal ionization mass spectrometer (TIMS) equipped with nine movable collectors. Sr and Nd isotope compositions were measured in dynamic mode and are reported normalized to $^{86}Sr/^{88}Sr = 0.1194$ and $^{146}Nd/^{144}Nd = 0.7219$, respectively. Exponential-law mass fractionation correction was used for all Sr and Nd isotopic data. Over the period of measurements, the external precision of NIST SRM987 was $^{87}Sr/^{86}Sr = 0.710255 \pm 7$ (2σ, $n = 10$), and that of Nd-Fi (in-house reference material) was $^{143}Nd/^{144}Nd = 0.511472 \pm 5$ (2σ, n = 10). These values are within error the long-term reproducibility of the two reference materials ($^{87}Sr/^{86}Sr = 0.710250 \pm 17$, 2σ, $n = 230$; $^{143}Nd/^{144}Nd = 0.511467 \pm 9$, 2σ, $n = 164$). The value of the in-house Nd reference material was calibrated with the La Jolla reference material (Avanzinelli et al., 2005) yielding $^{143}Nd/^{144}Nd = 0.511845 \pm 7$ (2σ, $n = 42$). Internal precision ($2\sigma_m$) for both Sr and Nd isotope measurements is typically ≤10 ppm.

4. Petrography and mineral chemistry

The FMN lamprophyre dyke shows a porphyritic texture with crystal/groundmass ratio between 15 and 25 vol%. The crystals consist of brownish amphibole (up to 3 cm in size; modal abundance up to 20 vol %), biotite (up to 7–8 vol%), ulvöspinel (<5 vol%) and apatite (~2 vol %) (Fig. 3). Biotite and amphibole contain polymineralic inclusions. The crystals grain size, with special reference to amphiboles, varies continuously from a maximum of 3 cm to less than 100 μm for crystals in the groundmass. The groundmass hosts feldspar clusters and rare xenoliths. According to the revised mineralogical lamprophyre classification of Lang et al. (2023) the FMN lamprophyre is a camptonite.

Macrocrystals: The amphibole macrocrysts occur in three different textural varieties: i) amphibole with concentric zoning (Fig. 3a), sometimes poikilitic on apatite and/or ulvöspinel; ii) unzoned amphiboles; iii) aggregate of amphiboles forming a glomeroporphyric texture. The largest amphibole crystals sometimes show resorption edges and embayments, testifying disequilibrium with the melt phase. The zoned amphiboles commonly show a wide, homogeneous core, either inclusion-free or crowded with several elongated and oriented needles of opaque minerals (Fig. 3b), and sometimes a corroded rim of ulvöspinel. In a few cases, medium-grained amphiboles almost completely replaced by opaque mineral aggregate were observed. Mineral inclusions observed in the amphibole comprise biotite, euhedral apatite, ulvöspinel, and carbonate (Fig. 3f). Inclusions of Mg—Fe spinel (ca. 500 μm in length), surrounded by a very thin layer of corundum, were also found in a single amphibole crystal from sample FZ11.

The biotite phenocrysts show comparable dimensions to those observed for amphiboles. In some samples, polymineralic inclusions rich in carbonate were also observed in biotite phenocrysts. Despite their relevant size, the biotite phenocrysts have a homogeneous composition. Often, the interface between the large biotite crystals and the surrounding groundmass is marked by a thin layer made up by the coalescence of several amphibole microcrystals (Fig. 3c).

Ulvöspinel occurs as euhedral to subhedral crystals up to 3–5 mm in size (Fig. 3d). It is rounded or polygonal in shape, sometimes characterized by a wide core up to 2 mm in size crowded with nanometric inclusions of a Ti-rich phase (rutile?), that is in turn surrounded by a thinner (half a millimeter) rim (Fig. 4a). The very thin outer rim resembles the microstructure of a reaction corona with nanometric blebs of ulvöspinel entering into the rock groundmass.

Apatite phenocrysts are smaller than amphibole, biotite, and ulvöspinel phenocrysts. They have been found as single crystals within the rock groundmass, in small clusters of apatite ± ulvöspinel (Fig. 3d), or associated to amphibole or biotite. Millimetric euhedral inclusions of apatite are often preserved inside the amphibole. More rarely, large and euhedral apatite crystals reaching half a centimeter in size have been observed in the groundmass.

Groundmass: The groundmass mainly consists of brownish

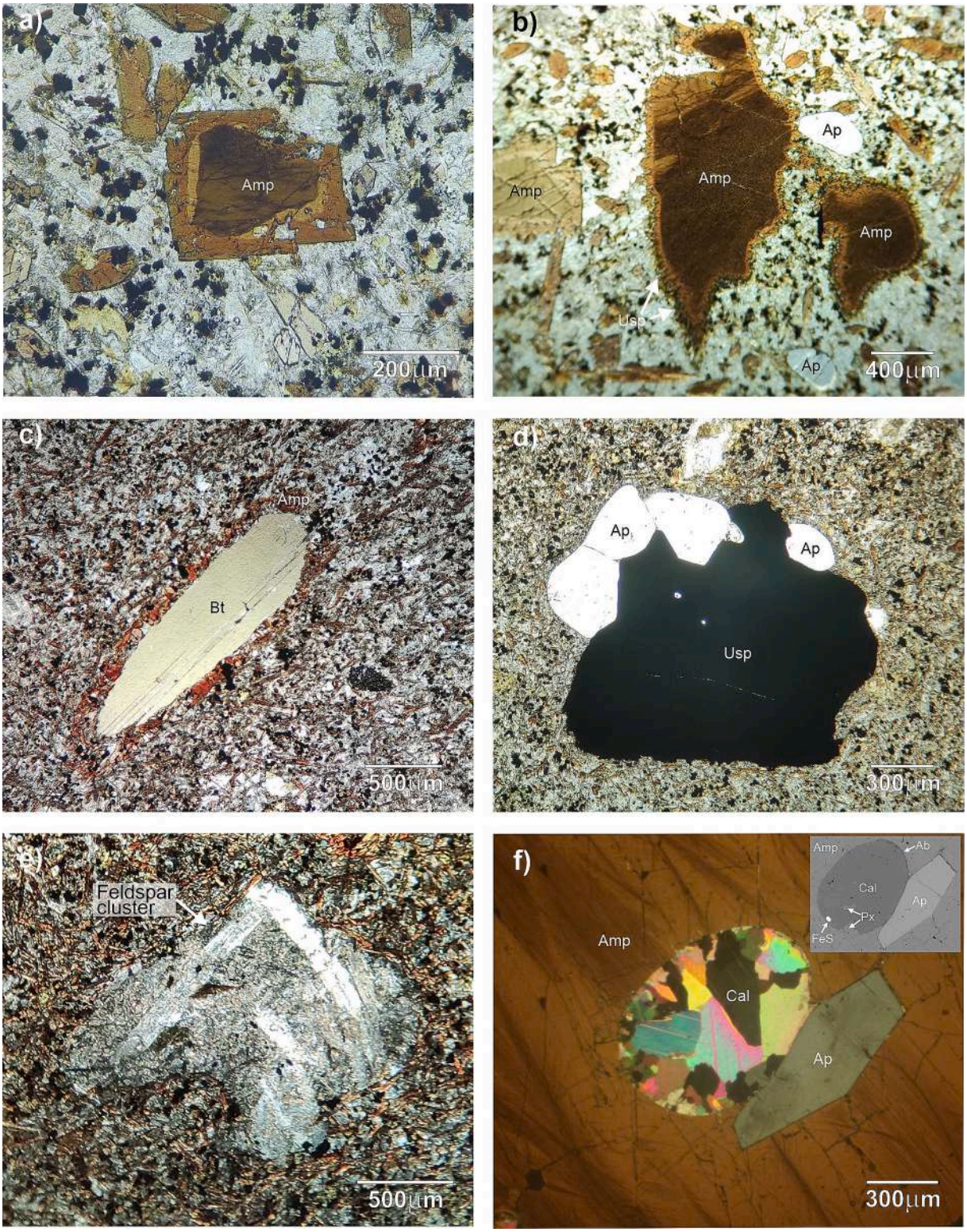

Fig. 3. Photomicrograph at the polarizing microscope showing microstructural features of the FMN lamprophyre. a) Amphibole compositional zoning; sample FZ7; b) Zoned amphibole with a wide core crowded with oriented needles of opaque minerals; sample FZ11; c) Large biotite surrounded by brownish amphibole resembling corona microstructure; sample FZ4; d) Ulvöspinel and apatite simulating a glomeroporphyric texture; sample FZ11; e) Feldspar cluster in the groundmass; Sample FZ4; f) Calcite-rich inclusion and euhedral apatite within amphibole; the inset in f) shows the same microstructure in BSE image; sample FZ7. Mineral abbreviations from Whitney and Evans (2010). FeS: Fe-sulphide.

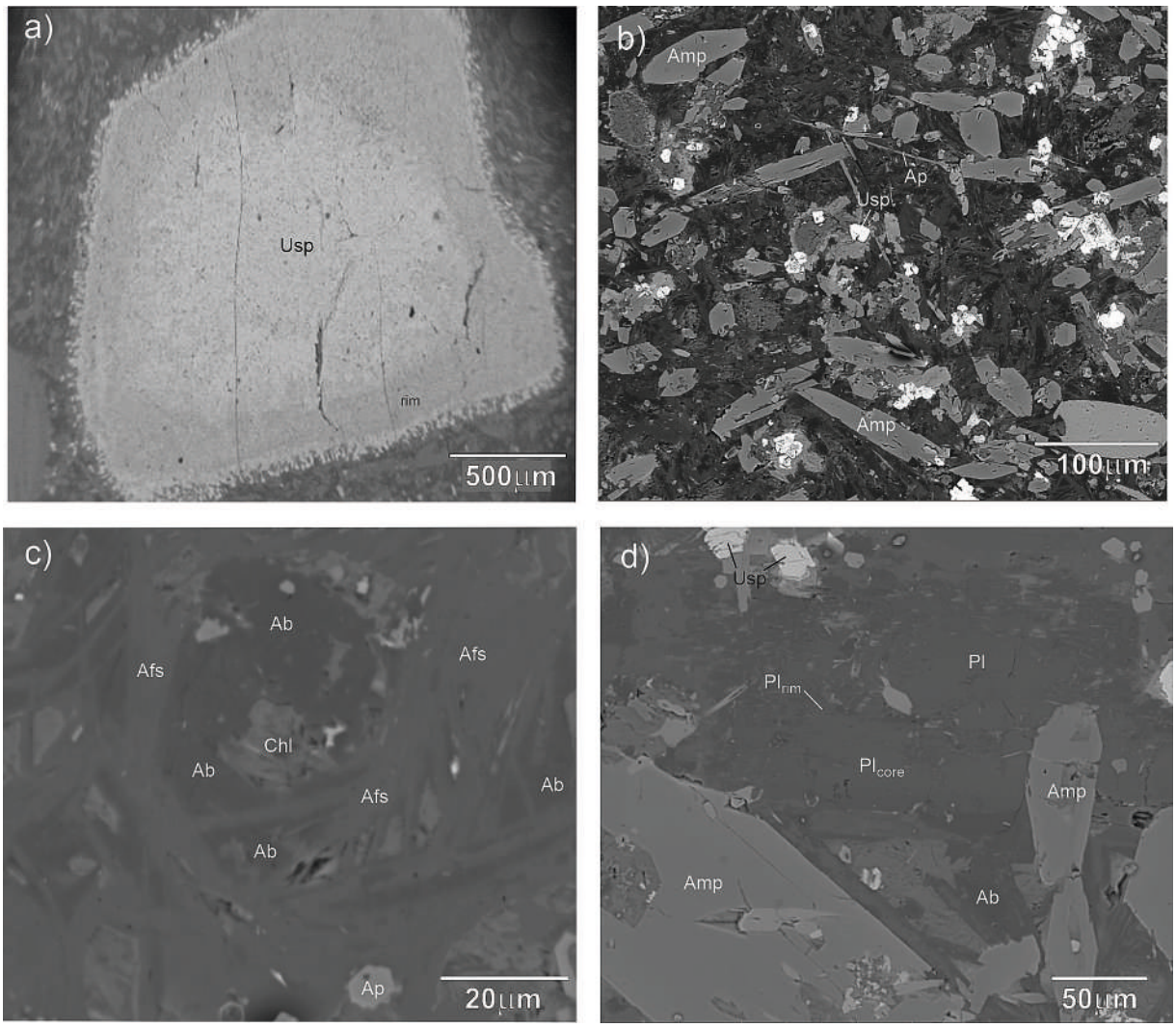

Fig. 4. Back-scattered electron images of selected microdomains of the FMN lamprophyre. a) Millimeter-sized ulvöspinel with a wide homogeneous core, surrounded by a rim with lower iron content and surrounded by a very thin, micrometric outer rim enriched in iron; sample FZ4; b) Groundmass made up of elongated amphibole microcrystals, acicular apatite and granular fine-grained ulvöspinel; sample FZ4; c) Alkali-feldspar/albite intergrowth and interstitial albite in the groundmass of sample FZ7; d) Zoned plagioclase in the lamprophyre groundmass; sample FZ7.

amphibole ± biotite + ulvöspinel microcrystals + apatite needles + feldspar clusters.

Amphiboles from the groundmass (100 to 200 µm in length) are optically zoned.

Ulvöspinel (Fig. 4b) is very fine-grained (ca. 20 µm) and sometimes contains nanometric inclusions of a TiO_2-rich phase, most probably rutile.

Apatite shows acicular shape; it occurs in needles with comparable length (100 to 200 µm) and significantly smaller thickness than the coexistent amphibole microcrystals (Fig. 4b).

Feldspar clusters (Fig. 3e) consist of an alternation/intergrowth of interstitial albite and alkali feldspar associated to rounded albite plagues (Fig. 4c), and prismatic, up to 100–150 µm in length. Slightly zoned plagioclase crystals (Fig. 4d). Plagioclase is sometimes rimmed by K-feldspar. In the FMN lamprophyre the occurrence of albite intergrown with K-feldspar suggests a late stage magmatic origin (Liu et al., 2023; Rock, 1991 and references therein).

Calcite sometimes associated with chlorite forms small patches into the rock groundmass.

Polymineralic inclusions: Spherical to subrounded polymineralic inclusions consisting of calcite and minor Fe—Cu sulphides and pyroxene are commonly found within amphibole (Fig. 3f). The boundary is marked by a very thin and discontinuous albite layer (Fig. 3f). Calcite has low MgO and BaO (up to 0.06 wt%) whereas MnO and SrO are up to 0.7 and 0.2 wt%, respectively (Table A1, Supplementary Material). The calcite composition is similar to that described by Vichi et al. (2005), which was interpreted as a primary mineral formed from a carbonatitic melt. Pyroxene (inset of Fig. 3f) is a compositionally zoned augite with X_{Mg} ratio of 0.54 in the core and an increase in hedenbergite component in the rim (X_{Mg} 0.39–0.41).

Polymineralic inclusions are found more rarely within biotite and mainly consist of calcite, with minor quartz, albite and Fe-sulphides. The albite forms a thin and discontinuous rim at the edge close to the contact with the surrounding biotite.

Xenolith nodules: The xenoliths are rounded to elongated greenish nodules up to a few centimeters in size (Fig. 2d), and consist of altered clinopyroxene, talc, chlorite, and calcite with accessory, submicron-sized Fe- and Ni-sulphides. The contact between the host lamprophyre and the xenolith nodules is sharp.

The microstructural features of a selected and representative centimetric xenolith nodule from sample FZ4 were investigated in detail (Fig. A1 of Supplementary Information). The nodule is composed of talc, growing on and surrounding clinopyroxene relics and chlorite patches. Talc (FeO 5.8–6.6 wt%), by far the most abundant mineral in the nodule,

occurs as single crystals surrounded by a fine network of talc microveins. Chlorite contains small amounts of chromium (0.5–1.0 wt% Cr_2O_3) and shows a composition variable between Fe- rich (FeO 26; MgO 21 wt%) and Mg- rich terms (FeO 19; MgO 25 wt%), with some chlorites showing compositional zoning. Locally, subordinate calcite, ulvöspinel and spinel have been observed at the boundary of the nodule, close or in contact with the rock groundmass (Fig. A1). Altered pyroxenes, characterized by the widespread growth of talc along their cleavage, are aluminian-diopside (X_{Mg} ratio ~ 0.90) with minor amounts of Ti, Mn and Na (Table A1, Supplementary Material). Although rare, strongly altered, and lacking fresh olivine, we interpret these nodules as mantle xenoliths brought to the surface by the ascending lamprophyre magma.

4.1. Mineral chemistry of the lamprophyre

Selected microprobe analyses of amphibole and biotite, together with analyses of groundmass mineral phases (feldspar, amphibole, biotite, and chlorite) from three selected lamprophyre samples are given in Table 1.

Amphibole: Structural formulae were calculated by the Amphibole Classification Excel Spreadsheet version 1.9.7 (Locock, 2014, last update August 2020), which takes into account the IMA recommendations for amphibole classification and nomenclature (Hawthorne et al., 2012). The W site occupancy was calculated as OH = $2\text{-}2^{C}$Ti a.p.f.u. (atoms per formula unit), considering the role of Ti in reducing the amount of OH required in the structural formula. Fe^{2+} and Fe^{3+} were calculated starting from an all-ferrous calculation and then correcting it if the cation sums were not consistent with mineral stoichiometry. The amphibole phenocrystals (including core and rim) and the cores of groundmass amphiboles are ferri-kaersutite (oxo-amphiboles group, Ca sub-group) with high TiO_2 contents (from 4.5 to 6.8 wt%). The rim of the groundmass amphiboles is Ti-rich magnesio-hastingsite (WOH-Cl-F-dominant amphiboles group).

The mineral chemistry of amphiboles was also examined for compositional zoning by means of X-ray mapping and compositional traverse; Mg, Mn, Ti, and Fe compositional X–ray maps of a selected amphibole from sample FZ7 are shown in Fig. 5, whereas rim–core–rim compositional profiles in terms of Mn, Ti, Fe and Mg (a.p.f.u.) across the same amphibole are reported in Fig. 6a. The amphibole in Fig. 5 shows a well-developed compositional zoning characterized by a wide (ca. 300–400 μm) and homogeneous Fe-rich/Mg-poor core, surrounded by a rim with increasing Mg and decreasing Fe. The rim is followed by an outer rim where Mg and Ti decrease and Fe increases. Other amphiboles have simpler zoning, consisting of a wide homogeneous Fe-rich/Mg-poor core surrounded by a thin rim enriched in Mg and Ti and depleted in Fe (Fig. A2). The small amphiboles in the groundmass show a compositional trend matching that observed for the rim and outer rim of the above-mentioned crystals (i.e., amphibole from groundmass lacks the compositional variations observed in the cores; see Fig. 5).

The composition of the amphiboles is diagnostic of alkaline and ultramafic lamprophyres (Fig. A3, after Rock, 1987; Rock, 1991). In the SiO_2 vs. TiO_2 diagram (Krmíček and Chalapathi Rao, 2021), the amphibole plot in the alkaline and ultramafic lamprophyre field, typical of anorogenic geodynamic settings (Fig. A3). Similar amphibole compositions have been documented in several European lamprophyres, from Southern Alps (Casetta et al., 2019; De Min et al., 2020), Ditrău Complex (Batki et al., 2014), Central Iberia (Orejana et al., 2008).

Biotite: Structural formulae were calculated following Li et al. (2020). All but one analyses plot on the phlogopite/annite fields, having a X_{Mg} ratio = 0.45–0.60 and Al_{tot} = 1.18–1.38 a.p.f.u. Biotite phenocrysts (X_{Mg}: 0.54–0.60) are not zoned and have high TiO_2 contents (7.06–7.5 wt%). Groundmass biotite contains lower amounts of titanium (3–4 wt%) and shows lower X_{Mg} ratio (0.45–0.50) in comparison to the phenocrystals.

Ulvöspinel: Zoned phenocrystals have an Fe-rich core (~ 65 FeO wt %) surrounded by a rim with lower Fe content (~ 60 FeO wt%). The rim is in turn surrounded by a micrometric outer rim, too small to be analyzed, again enriched in Fe (Fig. 4a). Titanium ranges from 0.3 to 0.6 a.p.f.u.. Low Si (0.01–0.08 a.p.f.u.), Al (0.03–0.3), Cr (<0.1), Mn (<0.07), and Mg (0.005–0.01) contents were also found. Higher Si (0.28 a.p.f.u.) and Mg (0.11) content was detected in the rim of the zoned ulvöspinel phenocrystal from sample FZ4. The micrometric, granular ulvöspinel in the groundmass shows a composition similar to that of the rim of the phenocrystals. The rare spinel included in an amphibole from sample FZ11 belongs to the spinel-hercynite series. It contains significant Cr content (Cr_2O_3 = 1.21 wt%; 0.026 a.p.f.u.) and low amounts of Mn (MnO = 0.17 wt%; 0.004 a.p.f.u.).

Apatite: The crystals are fluorapatite with 2 to 3 wt% F. Clorine content is low (0.2 wt%). Calcium is slightly replaced by Mn, more evident in apatite crystals (Mn = 0.02–0.03 a.p.f.u.) than in apatite occurring in the groundmass (Mn < 0.019 a.p.f.u.).

Feldspars: Two types of alkali-feldspars occur in the groundmass: an alkali feldspar with composition $Ab_{34–41}$, $Or_{58–66}$ and an almost pure K-feldspar with low Na ($Ab_{3–7}$).

Subhedral plagioclase in groundmass are compositionally zoned with andesine (An_{34}) core and oligoclase rim ($An_{21–27}$) (Fig. 6b). Anhedral albite was also found in the groundmass (Fig. 4c,d). Feldspars from clusters (i.e., plagioclase, alkali-feldspar and interstitial albite) have the same composition of those from the groundmass.

4.2. Trace elements in amphibole and biotite

Trace element and REE contents of selected core-rim amphibole and biotite crystals from samples FZ4 and FZ7 are reported in Table 2.

Amphibole: The amphibole outer rim domain is strongly enriched in Sr and Ba, as compared to core and rim. Vanadium is more abundant in the rim domains than in the cores; zirconium is depleted in the intermediate rim. The REE composition of the amphibole macrocrystal varies between the core, rim and outer rim domains. All the amphibole REE patterns are moderately fractionated with no significant Eu anomaly (Fig. A4). The REE abundance and pattern of the amphibole from sample FZ7 (Fig. 5) are comparable between the core and the outer rim, differing only by a slight enrichment in LREE (La, Ce, Pr) in the latter. The amphibole rim shows lower ΣREE (ΣREE: 78–84 ppm) than the other two domains (ΣREE: 146–157 ppm in the core; 171–218 in the outer rim) (see Table 2 and Fig. A4a). An amphibole from sample FZ4 shows similar trend and REE abundance between the core (ΣREE: 151–157 ppm) and the rim (ΣREE: 188–268 ppm), with very slight enrichment in LREE (La, Ce, Pr) in the rim (Fig. A4b).

Biotite: Rubidium, Sr and Ba range between 163 and 190, 292–349 and 4018–4776 ppm, respectively. Vanadium is significantly less abundant in sample FZ7 (76–91 ppm) than in sample FZ4 (156–180 ppm). Zirconium is <30 ppm. Most of the other elements (including REE) are below detection limits (Table 2).

5. Bulk rock chemistry

The analyzed FMN lamprophyre samples have very similar major and minor/trace elements compositions, indicating strong homogeneity within the dyke (Table 3).

The major element composition of FMN lamprophyre plot in the lamprophyre field of the MgO–K_2O–Al_2O_3 ternary diagram originally defined by Bergman (1987) and modified by Krmíček and Chalapathi Rao (2021), and is similar to the average composition of camptonite reported by Rock (1991). In particular, the FMN lamprophyre is characterized by similar contents of SiO_2, Al_2O_3, TiO_2, MnO, but lower MgO and CaO and higher K_2O, Fe_2O_3tot, P_2O_5 and CO_2. The K_2O/Na_2O ratio in the FMN lamprophyre ranges between 0.78 and 1.16. Moreover, all the samples plot in the transitional field of the K_2O vs. Na_2O diagram (Stoppa et al., 2014, Fig. 5a) with the exception of samples FZ2 and FZ3 that plot in the potassic field.

CIPW normative minerals (Table 3) indicate that the samples are

Table 1
Representative electron microprobe analyses of amphibole, biotite, apatite, ulvöspinel and feldspars from samples FZ7, FZ4, FZ11. Spinel inclusion in amphibole is also reported (sample FZ11). Amphiboles are ferri-kaersutite (Ferri-k) and Ti-rich magnesio-hastingsite (Ti-mg-h.).

FZ7	*Macrocrystals/ Phenocrystals*					*Groundmass*									
	Amphibole			Biotite	Apatite	Amphibole		Biotite	Ulvosp.	Apatite	K-feld.	Alk. Feld.	Plagioclase		Albite
	core	rim	out.rim			core	rim						core	rim	
SiO_2	39.04	39.08	38.89	35.01	–	37.92	38.07	35.65	1.72	–	65.12	66.45	59.89	62.70	67.77
TiO_2	4.59	6.69	5.50	7.49	–	6.58	3.84	3.21	14.89	–	0.10	0.04	–		–
Al_2O_3	12.92	12.40	13.02	14.94	–	13.20	14.09	12.75	0.66	–	18.92	19.11	24.69	23.22	19.88
Cr_2O_3	0.01	0.01	–	0.01	–	0.01	–	0.19	0.97	–	–	–	–		–
MnO	0.23	0.13	0.14	0.13	0.15	0.19	0.29	0.06	0.66	0.13	–	0.02	–		–
FeO	17.98	11.64	13.59	18.54	0.76	12.35	16.80	27.05	70.70	0.79	0.50	0.33	0.30	0.28	0.25
MgO	8.41	12.14	10.83	10.60	0.36	11.42	8.88	9.18	0.26	0.32	–	–	–		
CaO	10.04	12.28	11.67	0.02	52.58	11.85	11.55	–	–	52.77	–	0.52	6.48	4.50	0.01
Na_2O	2.82	2.48	2.51	0.83	–	2.52	2.58	0.42	–	–	0.78	4.72	7.16	8.11	11.35
K_2O	1.61	1.26	1.34	8.85	–	1.27	1.41	8.33	–	–	15.55	10.30	1.12	1.60	0.19
BaO	–	–	–	0.78	–	–	–	0.11	–	–	–	–	–	–	–
P_2O_5	–	–	–	–	40.89	–	–	–	–	41.20	–	–	–	–	–
F	–	–	–	–	2.55	–	–	–	–	1.91	–	–	–	–	–
Cl	–	–	–	–	0.27	–	–	–	–	0.26	–	–	–	–	–
Total	97.65	98.11	97.49	97.20	97.56	97.31	97.51	96.95	89.86	97.38	100.97	101.49	99.24	99.24	99.45
Si	5.978	5.866	5.907	2.736	–	5.751	5.829	2.774	0.069	–	2.976	2.974	2.680	2.779	2.977
Al	2.331	2.194	2.331	1.376	–	2.359	2.542	1.169	0.031	–	1.019	1.008	1.311	1.213	1.029
Ti	0.529	0.756	0.629	0.419	–	0.751	0.442	0.185	0.451	–	0.003	0.000	–	–	–
Cr	0.001	0.001	–	0.001	–	0.001	–	0.012	0.031	–	–	–	–	–	–
Mn	0.030	0.017	0.018	0.009	0.021	0.024	0.038	0.004	0.023	0.019	–	0.001	–	–	–
Fe^{3+}	1.084	1.136	0.929	0.280	–	1.231	0.912	0.584	0.898	–	0.017	0.012	0.010	0.009	0.008
Fe^{2+}	1.218	0.326	0.797	0.932	0.107	0.335	1.239	1.176	1.481	0.112	–	–	–	–	–
Mg	1.920	2.717	2.452	1.244	0.002	2.582	2.027	1.068	0.016	0.001	–	–	–	–	–
Ca	1.647	1.975	1.899	0.002	9.522	1.926	1.895	–	–	9.566	–	0.025	0.313	0.214	0.000
Na	0.837	0.722	0.739	0.126	–	0.741	0.765	0.063	–		0.069	0.410	0.625	0.697	0.967
K	0.314	0.241	0.260	0.871	–	0.246	0.275	0.836	–		0.906	0.588	0.064	0.090	0.011
Ba	–	–	–	0.024	–	–	–	0.003	–	–	–	–	–	–	–
P	–	–	–	–	5.851	–	–	–	–	5.902	–	–	–	–	–
F	–	–	–	–	1.363	–	–	–	–	1.022	–	–	–	–	–
Cl	–	–	–	–	0.077	–	–	–	–	0.075	–	–	–	–	–
O	1.057	1.511	1.257	0.960	–	1.501	0.885	0.451	–	–	–	–	–	–	–
OH	0.943	0.489	0.743	1.040	–	0.499	1.115	1.549	–	–	–	–	–	–	–
	Ferri-k.	Ferri-k.	Ferri-k.			Ferri-k.	Ti-mg-h.								

FZ4	*Macrocrystals/Phenocrystals*						*Groundmass*							
	Amphibole		Biotite	Ulvospinel		Apatite	Amphibole	Ulvosp.	Apatite	K-feld.	Alk. Feld.	Plagioclase		Albite
	core	rim		core	rim							core	rim	
SiO_2	38.99	38.48	34.89	0.45	7.57	–	38.45	0.50	–	65.30	65.11	61.13	62.52	68.77
TiO_2	4.51	6.85	7.31	20.69	13.48	–	5.50	17.30	–	0.20	–	–	–	–
Al_2O_3	12.89	12.80	14.98	5.36	6.85	–	13.23	5.31	–	18.80	18.30	24.10	23.11	19.38
Cr_2O_3	–	–	–	0.33	0.36	–	0.01	4.20	–	–	–	–	–	–
MnO	0.25	0.17	0.19	1.66	0.13	0.21	0.22	2.51	0.05	–	–	–	–	–
FeO	18.03	11.95	18.27	64.78	60.56	0.72	14.52	67.60	0.59	0.50	0.44	0.60	0.60	0.27
MgO	8.39	11.95	10.73	0.25	1.92	–	10.25	0.21	–	–	–	–	–	0.02
CaO	9.93	12.13	0.02	–	–	52.42	11.63	–	53.17	–	0.12	3.90	4.00	0.03
Na_2O	2.86	2.43	0.88	–	–	–	2.49	–	–	0.90	4.01	7.70	8.30	11.38
K_2O	1.68	1.36	8.78	–	–	–	1.32	–	–	15.43	11.88	1.90	1.50	0.19
BaO	–	–	0.77	–	–	–	–	–	–	–	–	–	–	–
P_2O_5	–	–	–	–	–	41.07	–	–	40.83	–	–	–	–	–
F	–	–	–	–	–	2.67	–	–	3.61	–	–	–	–	–
Cl	–	–	–	–	–	0.25	–	–	0.22	–	–	–	–	–
Total	97.53	98.12	96.82	93.52	90.87	97.34	97.62	97.63	98.47	101.13	99.86	99.33	100.03	100.04
Si	5.976	5.781	2.732	0.017	0.285	–	5.848	0.018	–	2.978	2.982	2.741	2.781	3.002
Al	2.329	2.267	1.383	0.241	0.304	–	2.371	0.228	–	1.011	0.988	1.274	1.212	0.997
Ti	0.520	0.774	0.410	0.594	0.382	–	0.629	0.476	–	0.007	–	–	–	–
Cr	–	–	–	0.010	0.011	–	0.001	0.122	–	–	–	–	–	–
Mn	0.032	0.022	0.013	0.054	0.003	0.030	0.028	0.078	0.007	–	–	–	–	–
Fe^{3+}	1.106	1.253	0.287	0.526	0.352	–	1.053	0.662	–	0.017	0.015	0.020	0.020	0.010
Fe^{2+}	1.206	0.249	0.909	1.544	1.555	0.101	0.794	1.405	0.082	–	–	–	–	–
Mg	1.917	2.677	1.259	0.014	0.108	–	2.324	0.011	–	–	–	–	–	0.001
Ca	1.631	1.953	0.002	–	–	9.468	1.895	–	9.506		0.006	0.188	0.191	0.001
Na	0.850	0.708	0.134	–	–	–	0.734	–	–	0.080	0.356	0.669	0.716	0.963
K	0.329	0.261	0.867	–	–	–	0.256	–	–	0.898	0.694	0.110	0.085	0.011
Ba	–	–	0.024	–	–	–	–	–	–	–	–	–	–	–
P	–	–	–	–	–	5.861	–	–	5.768	–	–	–	–	–
F	–	–	–	–	–	1.423	–	–	1.905	–	–	–	–	–
Cl	–	–	–	–	–	0.071	–	–	0.062	–	–	–	–	–
O	1.040	1.549	0.957	–	–	–	1.259	–	–	–	–	–	–	–

(*continued on next page*)

Table 1 (*continued*)

FZ4	*Macrocrystals/Phenocrystals*						*Groundmass*							
	Amphibole		Biotite	Ulvospinel		Apatite	Amphibole	Ulvosp.	Apatite	K-feld.	Alk. Feld.	Plagioclase		Albite
	core	rim		core	rim							core	rim	
OH	0.960 Ferri-k.	0.451 Ferri-k.	1.043	–	–	–	0.741 Ferri-k.	–	–	–	–	–	–	–

FZ11	*Macrocrystals/Phenocrystals*						*Groundmass*							*Inclusion*
	Amphibole			Biotite	Ulvosp.	Apatite	Amphibole		Ulvosp.	Apatite	K-feld.	Alk. Feld.	Plagioc.	Spl in Amp
	core	rim	out.rim				core	rim						
SiO_2	39.93	39.84	38.39	34.95	2.07	–	38.33	37.54	1.69	–	63.70	66.22	62.25	0.05
TiO_2	4.39	5.38	7.07	7.09	13.95	–	5.04	3.99	15.93	–	0.01	0.01	–	0.17
Al_2O_3	12.72	13.32	12.89	15.01	1.33	–	13.47	13.77	0.66	–	18.37	19.14	23.29	60.24
Cr_2O_3	–	–	–	–	0.01	–	0.01	0.01	0.22	–	–	–	–	1.21
MnO	0.21	0.14	0.16	0.12	0.39	0.13	0.29	0.33	0.65	0.01	–	0.08	–	0.17
FeO	16.92	11.61	12.32	18.92	73.52	0.80	16.34	19.10	70.92	0.72	0.18	0.22	0.32	24.08
MgO	9.05	12.46	11.39	10.97	0.19	0.38	8.98	7.22	0.09	–	–	–	–	13.86
CaO	10.17	10.83	12.20	0.03	–	52.17	11.69	11.45	–	53.17	0.06	0.24	4.41	–
Na_2O	2.77	2.59	2.42	0.78	–	–	2.52	2.47	–	–	0.43	4.47	8.15	–
K_2O	1.86	1.78	1.35	8.84	–	–	1.28	1.36	–	–	16.19	11.01	1.75	–
BaO	–	–	–	0.71	–	–	–	–	–	–	–	–	–	–
P_2O_5	–	–	–	–	–	41.04	–	–	–	41.64	–	–	–	–
F	–	–	–	–	–	2.82	–	–	–	2.67	–	–	–	–
Cl	–	–	–	–	–	0.28	–	–	–	0.21	–	–	–	–
Total	98.02	97.95	98.19	97.42	91.46	97.62	97.95	97.24	90.16	98.42	98.94	101.39	99.24	99.78
Si	6.068	5.925	5.788	2.721	0.081	–	5.866	5.840	0.068	–	2.982	2.972	2.770	0.001
Al	2.278	2.335	2.290	1.377	0.062	–	2.429	2.525	0.031	–	1.014	1.013	1.222	1.903
Ti	0.502	0.602	0.802	0.395	0.413	–	0.580	0.467	0.482	–	0.000		–	0.003
Cr	–	–	–	–	0.000	–	–	–	0.007	–	–	–	–	0.026
Mn	0.027	0.018	0.021	0.008	0.013	0.019	0.038	0.043	0.022	0.001	–	0.003	–	0.004
Fe^{3+}	0.946	1.108	1.198	0.295	0.949	–	0.902	0.894	0.863	–	0.006	0.007	0.011	–
Fe^{2+}	1.203	0.336	0.355	0.937	1.471	0.113	1.189	1.591	1.522	0.100	–	–	–	0.540
Mg	2.050	2.762	2.560	1.271	0.011	0.020	2.049	1.674	0.005	–	–	–	–	0.554
Ca	1.656	1.726	1.971	0.003	–	9.427	1.917	1.909	–	9.487	0.003	0.012	0.210	–
Na	0.817	0.747	0.708	0.118	–	–	0.748	0.745	–	–	0.039	0.389	0.703	–
K	0.361	0.338	0.260	0.869	–	–	0.250	0.270	–	–	0.967	0.630	0.099	–
Ba	–	–	–	0.022	–	–	–	–	–	–	–	–	–	–
P	–	–	–	–	–	5.860	–	–	–	5.871	–	–	–	–
F	–	–	–	–	–	1.504	–	–	–	1.406	–	–	–	–
Cl	–	–	–	–	–	0.080	–	–	–	0.059	–	–	–	–
O	1.004	1.204	1.604	0.903	–	–	1.161	0.934	–	–	–	–	–	–
OH	0.996 Ferri-k.	0.796 Ferri-k.	0.396 Ferri-k.	1.097	–	–	0.839 Ti-mg-h.	1.066 Ti-mg-h.	–	–	–	–	–	–

SiO_2-undersaturated, with nepheline content ranging from 0.39 to 3.78 wt%.

According to the TAS diagram and the normative olivine content (19.6–22.0 wt%), the studied samples can be classified as basanites and have the strongest alkaline affinity among European Permo-Triassic lamprophyres (Fig. 7a). The $Mg/(Mg + Fe^{2+})$ ratio ranges between 0.48 and 0.50.

Based on the Al_2O_3–MgO–CaO diagram (Rock, 1991), all samples fall in the Alkaline Lamprophyres (AL) fields (Fig. 7b). The composition of Permian-Triassic lamprophyres from different European regions is also reported for comparison. Lamprophyres from this study are similar to those from Carpathians, Romania (Ditrău Complex, Batki et al., 2014) and Central-Iberian Zone (Orejana et al., 2008; Scarrow et al., 2011). Lamprophyres from Southern Alps (Dolomitic Area, Casetta et al., 2019) partly overlap the FMN lamprophyre, although higher CaO and lower Na_2O contents (Alpine samples) are observed.

The incompatible trace element patterns, normalized to primitive mantle (McDonough and Sun, 1995) show weak positive anomalies of Ba, Nb, K and P and weak negative anomalies of Th and Ta (Fig. 7c). The patterns and elemental concentrations of the FMN lamprophyres mimic the average AL composition (Rock, 1991), although slight differences are observed in terms of positive K and P anomalies (Fig. 7c).

The comparison with the above-mentioned European camptonites shows similar trends, always consistent with the average AL composition (Rock, 1991), with a general decrease of normalized concentrations towards the less incompatible elements. However, other European lamprophyres tend to exhibit, on average, slight lower trace element content than the FMN lamprophyres. The Pb content of the FMN samples, shows no or only slightly negative anomaly (Fig.7c), resembling that of samples from Carpathians and Central-Iberian Zone. In the Th–Hf–Nb/2 discrimination diagram (Krmíček and Chalapathi Rao, 2021), all European camptonites plot close to the AL average composition (Fig. A5).

Chondrite-normalized REE patterns are characterized by a constant fractionation from light REEs (more enriched) to heavy REEs and by the absence of Eu anomaly (Fig. 7d). The Ce_N/Yb_N ratio, ranging between 13.6 and 14.4 indicates a significant REE fractionation more marked in LREE (La_N/Sm_N = 3.2–3.6) than in HREE (Gd_N/Yb_N = 2.9–3.3). This pattern is a common characteristic of all European camptonites (Fig. 7d). An almost perfect overlap between the REE patterns of FMN lamprophyres and the average AL (Rock, 1991) can be observed from La to Tb, even though Sardinian samples tend to be slightly enriched in HREE.

Initial Sr and Nd isotope compositions of FMN lamprophyres are reported in Table 4. The Nd isotope composition of all European lamprophyres, except those from Central Iberia and one sample from Southern Alps (De Min et al., 2020), are clustered close to the Enriched Depleted Morb Mantle (*E*-DMM, Workman and Hart, 2005) composition at 220 Ma (Fig. 8). The Sr isotope compositions of the Carpathians lamprophyres are displaced towards unreasonably low values likely due to Rb gain during hydrothermal alteration (Batki et al., 2014), whereas the Southern Spain lamprophyres are displaced towards more

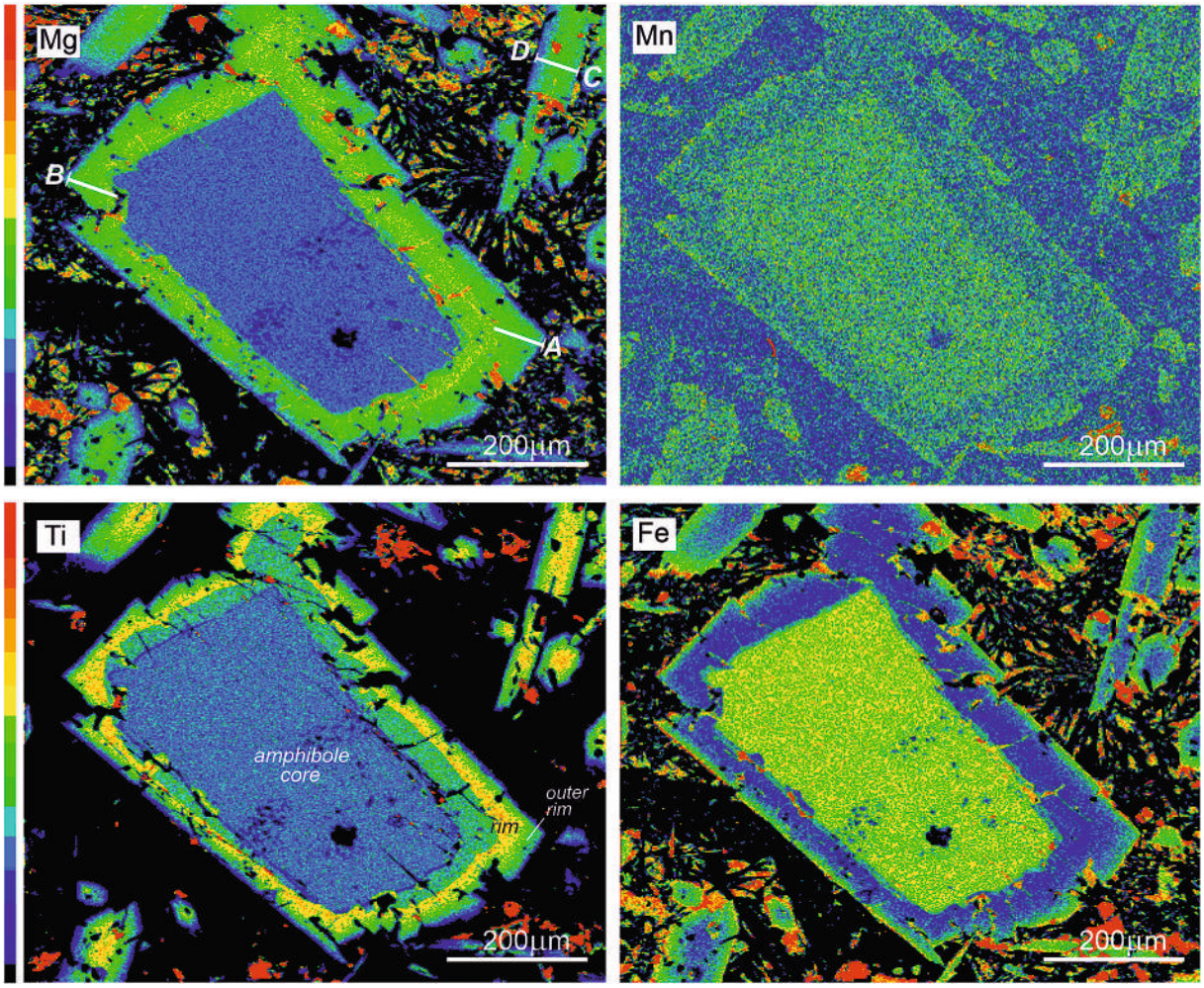

Fig. 5. X-ray Mg, Mn, Ti and Fe concentration maps of an amphibole from sample FZ7; Traces A–B and C–D in the Mg-map show the compositional profiles of Fig. 6a, b. The groundmass amphiboles do not show the core domain. Warm colours refer to high concentrations, cold colours refer to low concentrations (scales for the colour code on the left-hand side of the maps).

radiogenic Sr isotope compositions due to, perhaps, sea water alteration (Puga et al., 2010). Overall, the relatively high and homogeneous Nd isotope compositions of most European lamprophyres are typical of enriched intra-plate magmas and are comparable to values observed in continental alkaline volcanic suites from extension and rift settings (e.g., Tappe et al., 2006). The Central Iberia lamprophyres and the sample from Southern Alps define a separate cluster close to the Bulk Silicate Earth (BSE) composition (Fig. 8), which is, however, always compatible with continental alkaline volcanic suites.

We also reported in Fig. 8, the radiogenic isotope compositions of samples from Triassic alkaline dykes in the Ivrea-Verbano Zone (Ogunyele et al., 2024; Stähle et al., 2001), along with samples from the Finero-Balmuccia phlogopite-bearing peridotite (Voshage et al., 1987), and mafic intrusive rocks from the Ivrea-Verbano Zone and the Palaeozoic Sardinia basement (CSB in Fig. 8, data from Voshage et al., 1987; Tommasini et al., 1995; Franciosi et al., 2019; Secchi et al., 2022). The radiogenic isotope signature of these samples will be considered in the following discussion on the mantle source of the FMN lamprophyres.

6. Amphibole crystallization P-T conditions

The crystallization conditions of amphibole can be roughly estimated using the Amp-TB2 algorithm (Ridolfi, 2021), which allows calculating P, T, and volatile content in the melt during steady-state crystallization of calcic amphiboles. The results of this method applied to the two textural types of amphiboles (i.e. macrocrystals and matrix amphibole) are given in Table 5. The deeper crystallization conditions are determined using the composition of the wide, homogeneous Fe-rich/Mg-poor core of the amphibole. However, due to the high Fe and low Mg content of amphibole cores, the P-T results should be interpreted with caution. The core composition yields T in the range 991–1032 °C and P in the range 962–1244 MPa. Rim crystallization conditions indicate slightly higher temperature (ranging between 1039 and 1072 °C) but significantly lower pressure (range: 913–488 MPa). Amphiboles from the groundmass show temperatures (within 1009–1065 °C) comparable to those recorded by the rim of the amphibole macrocrystals, but, on average, they record lower pressures (510–760 MPa).

These results are consistent with the observation that amphibole macrocrystals cores exhibit higher K_2O and lower TiO_2 concentrations than the groundmass crystals (Table 1), indicating that the wide amphibole cores crystallized under higher pressure conditions than microcrysts (Shaw and Eyzaguirre, 2000).

The calculated ranges are also consistent with the experimental simulations conducted by Pilet et al. (2010), who demonstrated that kaersutite crystallization can start at 1130 °C and 1.5 GPa in volatile-rich basanitic melts. These results suggest that crystallization of the lamprophyre occurred between ca. 1.15 and 0.5 GPa, with T decreasing from >1100 to ~1000 °C, with an H_2O content >5 ± 0.9 wt%. Moreover, they support the hypothesis of two crystallization levels: one at the mantle-crust boundary and another at the boundary between the lower

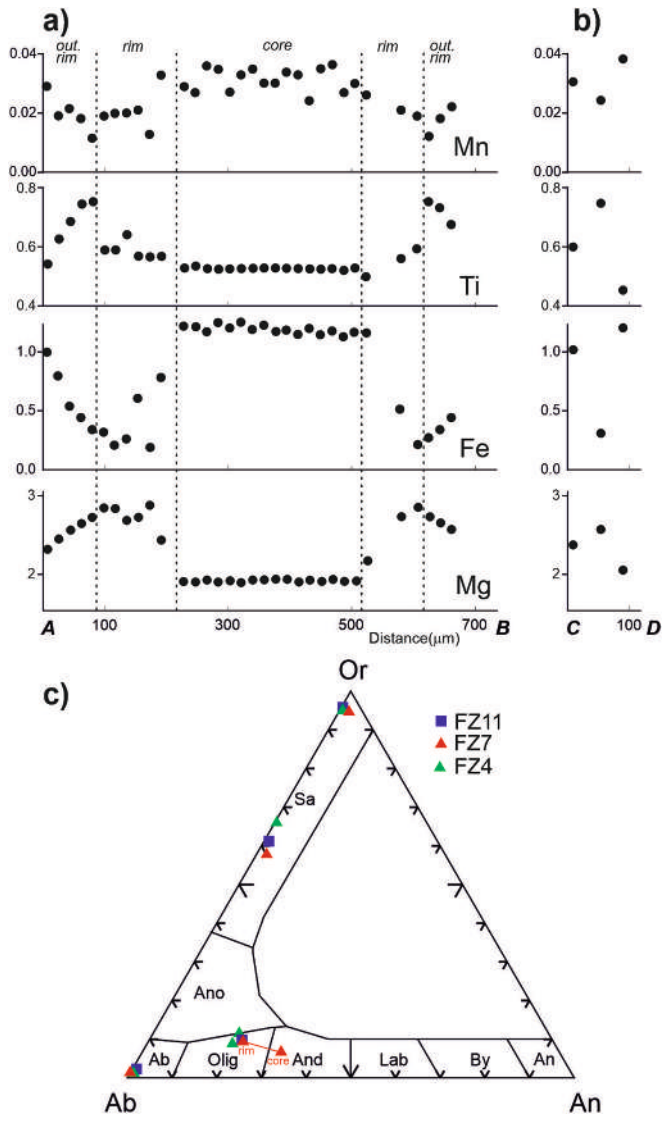

Fig. 6. (a) Rim-core-rim compositional profile across the A-B trace of the zoned Fe-kaersutite mapped in Fig. 5; (b) Compositional profile across the C–D trace of the matrix amphibole in Fig. 5; (c) Composition of feldspars of the FMN lamprophyre in the orthoclase (Or)–albite (Ab)–anorthite (An) ternary diagram. Mineral abbreviations from Whitney and Evans (2010). Olig: oligoclase, And: andesine; Lab: labradorite; By: bytownite.

and upper crust.

Further attempts to estimate the P-T conditions of amphibole formation were performed using the algorithm of Putirka (2016), which, in addition to amphibole composition, considers the composition of the coexisting melt. Different liquid compositions were assumed, starting from bulk rock, and then subtracting 10, 20 or 30 % of amphibole, biotite and ulvöspinel phenocrysts according to their relative modal amounts. Further calculations were performed changing the H_2O content in the melt, from 5 wt% (estimated by the hygrometer of Ridolfi, 2021) to 10 wt%. In each calculation, both T and P vary widely, without systematic differences between core and rim analyses. In addition, the different equations used for the P-T calculations (Putirka, 2016; Ridolfi, 2021) are commonly in disagreement. The inconsistency of these calculations is due to the difficulty in estimating the melt composition but it is also linked to the strong disequilibrium between amphibole and coexisting melt. All the assumed liquid compositions result in exchange coefficients $K_D(Fe—Mg)^{Amp–Liq}$ (hereafter K_D) higher than equilibrium values $K_D = 0.28 \pm 0.11$ (Putirka, 2016). Cores record the highest values ($K_D = 0.79–0.92$) suggesting a strong disequilibrium with the coexisting melt, whereas rims and small amphibole in the matrix yielded $K_D = 0.36–0.68$. Amphibole cores far from equilibrium followed by more equilibrated rims is fully supported by the textural evidence and has already been described in similar lamprophyres by Casetta et al. (2019).

7. Discussion

7.1. Magmatic processes: Constraints from amphibole texture

The FMN lamprophyre amphibole crystals show an increase in Mg (and decrease in Fe) from core to rim, followed by a decrease in Mg (and increase in Fe) towards the outer rim (Fig. 5). Consequently, the Mg# increases from core to rim followed by a decrease from rim to outer rim. The composition of the wide, homogeneous, Fe-rich/Mg-poor core of the amphibole is thus a more evolved composition, with Mg# values lower than all the other crystal domains. This observation, together with textural evidence from several macrocrystals (i.e., partially resorbed, anhedral, rounded habitus of the wide inner core, Fig. 3a, b; A2) suggests that the amphibole cores can be considered antecrysts (as defined by Ubide et al., 2014), which mostly crystallized from an evolved magma in the deep crust. The increase in MgO content from cores to the rims (MgO from 8 to 12 wt%, Table 1) likely reflects a recharge event by a more primitive magma (Casetta et al., 2019; Serre et al., 2020; Ubide et al., 2014). The partially resorbed amphiboles with black, altered core crowded with numerous needles of opaque minerals (Fig. 3b) are similar to the type 4 amphiboles described by Casetta et al. (2019, see their fig. 7d) in the Predazzo lamprophyre, Southern Alps. These authors interpreted type 4 amphiboles as relicts of larger crystals of deep crustal origin, brought to the surface by the magma ascent. Alteration and partial resorption of these amphibole cores implies disequilibrium with the coexisting melt, whereas the rims may represent a late overgrowth approaching equilibrium.

REE patterns normalized to chondrites (Fig. A4) are slightly convex upward and show an enrichment of LREE over HREE. The lack of Eu anomaly indicates that amphibole crystallized prior to feldspars (Casetta et al., 2019; Serre et al., 2020; Torres García et al., 2020). REE contents in amphibole macrocrystals vary from one zone to another but share the same pattern. Core analyses show lower REE compared to the outer rims; this behaviour can be explained by the low compatibility of REE in amphibole, resulting in REE "exclusion" from early forming crystals and a greater incorporation during the later growth (Serre et al., 2020). In addition, it has been demonstrated that partition coefficients of REE between amphibole and melt are inversely correlated to pressure (Adam and Green, 1994), thus, the decompression after core formation, would result in REE enrichment in the rim. However, these explanations do not account for the strongest REE depletion in the inner rims (Fig. A4a), already observed in similar context (e.g., Ubide et al., 2014). We can hypothesize that the magma injection occurred after core growth (diluting the budget of REE available in the melt) or that some other phases (e.g., apatite) crystallized prior to rim formation, reducing the REE contents in the melt. Alternatively, the enrichment in REE from rim to outer rim can be interpreted as the result of fractional crystallization of amphibole from the melt, whereas the distinct composition of the core reflects its non-cogenetic origin relative to the rim, consistent with an antecryst interpretation.

7.2. Nature of the mantle source

Although lamprophyres often occur as small-volume outcrops, their distinctive geochemical features make them valuable for reconstructing large-scale geodynamic scenarios. The FMN lamprophyre has a major element composition typical of basanite, although olivine is absent and pyroxene only occurs as inclusions (Fig. 3f), replaced by a volatile-rich paragenesis, mainly consisting of Ti-rich biotite and amphibole (ferri-kaersutite, magnesio-hastingsite).

Table 2
Trace-elements and REE composition of different textural types of amphibole and biotite from samples FZ7 and FZ4.

	Amp_{core}	Amp_{core}	Amp_{core}	Amp_{core}	Amp_{rim}	Amp_{rim}	$Amp_{o.rim}$	$Amp_{o.rim}$	Bt	Bt	Amp_{core}	Amp_{core}	Amp_{rim}	Amp_{rim}	Bt_{core}	Bt_{rim}
Sc	26.05	25.93	26.24	25.17	42.78	34.25	66.34	34.37	3.90	3.29	27.04	24.11	39.59	71.31	4.07	4.88
Rb	6.91	6.34	5.95	6.54	6.39	4.73	4.29	4.08	163.61	183.09	5.84	6.88	14.14	15.26	180.09	190.89
Sr	766.0	806.5	799.1	826.7	601.9	517.6	1440.0	1634.7	292.2	349.4	797.2	807.1	1184.9	1313.1	301.4	332.8
Y	25.01	27.04	27.73	25.90	18.53	16.56	32.68	34.46	0.24	0.23	26.67	27.69	33.08	30.60	bdl	0.13
Nb	62.49	67.71	68.79	66.76	28.50	29.65	93.13	128.49	37.86	47.07	66.52	67.24	122.46	78.14	29.47	32.29
Ba	230.6	235.6	235.3	247.1	236.1	214.4	684.8	799.0	4018.5	4776.6	220.8	244.6	634.7	619.9	4157.7	4451.1
La	15.42	15.81	15.85	16.22	7.93	7.07	19.63	25.70	0.11	0.06	15.98	17.77	43.26	21.87	bdl	bdl
Ce	50.30	51.17	50.25	53.84	26.69	25.65	60.88	79.75	0.21	0.11	54.34	55.03	102.31	64.59	bdl	bdl
Pr	8.21	8.71	8.91	8.59	4.75	4.11	9.23	11.45	0.04	bdl	8.40	7.80	12.77	9.44	bdl	0.03
Nd	38.40	44.75	37.34	40.55	22.05	16.89	43.43	53.50	0.18	bdl	37.45	41.71	59.75	48.59	bdl	bdl
Sm	8.85	9.87	9.54	9.47	5.22	5.41	7.63	14.28	bdl	bdl	9.56	7.46	13.35	10.53	bdl	bdl
Eu	3.23	3.45	3.52	3.08	1.97	2.53	3.92	4.41	0.15	0.16	3.58	2.05	4.58	3.68	0.07	0.27
Gd	7.74	7.14	7.97	10.53	5.28	5.70	10.42	11.76	bdl	0.09	8.02	9.68	10.94	10.71	bdl	bdl
Tb	1.07	1.28	1.36	0.99	0.66	0.53	1.27	1.62	bdl	bdl	1.06	1.48	1.69	1.42	bdl	bdl
Dy	6.60	6.34	6.42	6.89	5.40	4.02	7.04	7.96	bdl	0.05	5.99	5.94	8.94	9.29	bdl	0.13
Ho	1.09	1.16	0.70	1.13	0.80	0.50	1.25	1.36	bdl	bdl	0.84	1.47	1.42	1.42	bdl	bdl
Er	2.83	4.14	3.89	2.35	1.47	1.69	3.89	2.62	bdl	bdl	2.28	3.45	4.36	2.87	0.15	bdl
Tm	0.34	0.22	0.45	0.43	0.41	0.28	0.41	0.56	0.02	0.01	0.54	0.33	0.61	0.41	bdl	bdl
Yb	2.09	3.06	2.25	2.32	1.22	2.90	1.56	3.02	0.06	bdl	2.48	3.02	3.68	3.45	0.28	0.39
Lu	0.299	0.125	0.384	0.201	0.101	0.218	0.331	0.352	bdl	bdl	0.497	0.285	0.417	0.196	0.035	bdl
Hf	4.16	4.63	4.52	5.73	2.49	1.37	6.40	7.98	0.71	0.21	3.30	5.09	6.25	6.96	0.69	0.48
Ta	3.45	2.86	3.05	3.37	1.78	2.62	4.87	7.19	1.61	1.95	3.46	3.99	6.51	5.53	1.48	2.15
Th	0.060	0.063	0.137	0.119	0.041	0.119	0.055	0.308	0.041	bdl	0.103	0.066	1.370	0.717	bdl	bdl
Ti	3250.0	3191.2	3163.4	3310.3	3680.8	3173.3	4831.2	4612.6	4177.6	5130.9	3235.3	3279.1	3803.6	4439.9	4849.0	5110.8
K	8979.1	8593.9	8580.1	9029.4	9044.5	7545.1	7113.6	6865.0	34,421.2	40,341.3	8497.7	8779.7	8236.3	7551.8	44,532.4	46,129.8
Mn	1788.0	1861.2	1856.2	1941.4	943.9	932.2	1142.5	1194.9	841.7	1054.0	1785.0	1846.3	1094.9	1090.9	794.7	821.9
V	113.5	115.2	120.5	121.5	458.8	405.8	321.9	247.4	76.2	91.5	113.9	116.6	174.4	286.6	155.9	180.8
Cr	bdl	bdl	bdl	bdl	787.86	641.85	20.13	bdl	bdl	bdl	bdl	bdl	bdl	bdl	45.54	58.24
Zr	138.90	143.51	151.11	159.56	82.35	79.43	194.56	240.39	25.20	20.23	150.03	156.39	262.75	210.86	14.43	13.73
U	0.022	bdl	0.040	bdl	0.096	0.026	0.096	0.127	0.029	0.012	0.032	0.093	0.345	0.032	0.030	bdl
ΣREE	146	157	149	157	84	78	171	218	0.79	0.50	151	157	268	188	0.53	0.83

Table 3
Major elements, CIPW norm, and trace element concentration of some selected samples of the lamprophyre dyke.

Sample	FZ1	FZ2	FZ3	FZ4	FZ7	FZ8	FZ9	FZ10	FZ11
SiO_2	43.33	42.94	43.21	41.79	42.62	43.36	42.23	43.05	41.76
TiO_2	2.67	2.60	2.64	3.04	2.8	2.90	2.74	2.67	2.98
Al_2O_3	14.75	14.72	14.85	14.21	14.28	14.88	14.42	14.63	14.28
Fe_2O_{3tot}	13.31	12.88	13.03	14.70	13.66	14.06	13.57	13.31	14.20
Cr_2O_3	0.01	0.02	0.01	0.02	0.02	0.01	0.01	0.02	0.01
MnO	0.15	0.17	0.18	0.18	0.22	0.17	0.19	0.19	0.17
MgO	5.52	5.12	5.22	5.68	6.33	5.41	5.65	5.92	5.33
CaO	6.68	7.42	7.38	7.58	7.67	7.40	7.89	7.38	8.04
Na_2O	3.53	3.29	3.23	3.31	3.29	3.65	3.58	3.35	3.43
K_2O	3.12	3.82	3.63	3.15	3.03	3.32	2.78	3.29	3.13
P_2O_5	1.58	1.57	1.53	1.65	1.52	1.63	1.53	1.47	1.52
LOI	4.97	4.96	4.09	4.21	4.01	4.75	4.16	4.29	4.57
CO_2	2.09	2.78	2.45	2.47	2.51	2.42	2.33	2.18	2.60
CIPW Norm									
Or	19.26	23.46	22.27	19.26	18.49	20.03	17.13	20.21	19.21
Ab	30.49	25.84	26.03	24.96	26.13	26.28	25.53	24.61	23.13
An	10.06	9.33	11.54	11.59	12.71	10.99	15.06	13.72	14.15
Nph	0.39	1.67	1.29	2.20	1.43	2.81	3.30	2.61	3.78
Crn	2.13	1.95	1.59	1.30	1.11	1.36	0.24	0.73	0.28
Ol	20.51	19.34	19.63	21.60	22.02	20.28	20.95	21.15	20.57
Ilm	5.29	5.12	5.20	5.98	5.48	5.62	5.43	5.26	5.88
Mag	3.03	2.91	2.94	3.30	3.07	3.11	3.08	3.00	3.20
Ap	3.82	3.77	3.68	3.96	3.63	3.84	3.70	3.54	3.64
Cal	4.98	6.57	5.79	5.82	5.89	5.61	5.52	5.13	6.14
V	139	133	135	157	156	155	143	138	157
Ga	20.1	19.5	20.2	21.4	20.3	21.0	20.6	20.2	19.8
Rb	57.5	77.7	72.7	59.1	51.9	70.9	50.6	59.7	63.7
Sr	1030	1260	1185	1275	962	1325	1130	1080	1190
Y	30.4	29.4	30.6	32.3	30.0	31.8	29.9	29.3	29.9
Zr	339	333	328	331	311	346	316	306	319
Nb	76.8	76.8	77.9	79.0	73.4	80.3	76.0	73.6	75.0
Sn	3.0	2.0	2.3	3.0	2.1	3.0	2.2	1.9	2.0
Cs	2.08	3.55	3.38	2.65	1.22	7.78	2.27	2.53	4.17
Ba	772	1065	1035	848	729	775	654	796	695
Hf	6.7	6.6	7.0	6.7	6.7	6.6	6.6	6.5	6.2
Ta	3.2	3.3	4.5	2.6	4.1	3.0	4.4	4.3	2.4
W	1.4	1.6	1.6	1.7	1.6	1.5	1.5	1.5	1.8
Th	5.29	5.37	5.91	4.95	5.41	5.45	5.66	5.50	5.04
U	1.80	1.88	1.98	1.79	1.82	1.92	1.90	1.88	1.76
Pb	8.0	7.5	9.0	8.3	7.0	6.7	6.5	8.0	8.7
La	61.5	60.9	61.5	62.1	57.0	63.7	59.6	58.0	58.0
Ce	122	121	126	127	122	127	124	120	118
Pr	14.10	13.75	14.80	14.65	14.20	14.55	14.45	13.95	13.50
Nd	57.4	58.1	57.1	61.3	54.8	60.2	55.8	54.2	56.6
Sm	10.70	10.55	10.25	12.05	10.20	11.30	10.10	9.86	11.05
Eu	3.20	2.95	2.97	3.20	3.07	3.22	3.00	2.92	3.16
Gd	8.67	8.34	8.55	9.39	8.33	9.23	8.46	8.10	9.04
Tb	1.22	1.15	1.18	1.32	1.18	1.24	1.15	1.08	1.16
Dy	5.99	5.92	6.26	6.67	6.12	6.64	6.03	5.87	6.47
Ho	1.14	1.12	1.17	1.26	1.19	1.22	1.14	1.12	1.15
Er	2.92	2.80	3.07	3.02	3.00	2.92	2.85	2.85	2.91
Tm	0.38	0.38	0.39	0.44	0.38	0.41	0.39	0.37	0.36
Yb	2.36	2.33	2.40	2.33	2.37	2.46	2.26	2.27	2.27
Lu	0.36	0.35	0.36	0.37	0.32	0.38	0.34	0.34	0.37

The initial radiogenic isotope compositions of the FMN lamprophyre (5 samples, Table 4), along with other European lamprophyres, provide robust constraint on their mantle source. As a whole, they can be divided in two groups (Fig. 8): the first group, consisting of the FMN lamprophyre along with those from Carpathians, Southern Alps, and Southern Spain, is characterized by homogeneous $^{143}Nd/^{144}Nd_i$ (ca. 0.5126–0.5127) and variable $^{87}Sr/^{86}Sr_i$ (ca. 0.701–0.706) due to Rb gain (Romania) and sea-water alteration (Southern Spain); the second group, consisting of the Central Iberia lamprophyres and one sample from the Southern Alps, exhibits unradiogenic Nd isotope composition (ca. 0.5122–0.5123) and a more restricted Sr isotope composition (0.704–0.705).

The relatively high initial Nd isotope composition of the first group rules out the subcontinental lithospheric mantle as their source region. This is demonstrated by the radiogenic Sr isotope and unradiogenic Nd isotope composition of the Finero-Balmuccia phlogopite-bearing peridotite and the mafic intrusive rocks from the Ivrea-Verbano Zone and the Palaeozoic Sardinia basement (Fig. 8), the latter two set of samples considered a *proxy* of the subcontinental lithospheric mantle metasomatized during the Ordovician subduction and subsequent Hercynian orogeny leading to the building up of the Pangea supercontinent (e.g., Ogunyele et al., 2024; Stähle et al., 2001; Tommasini et al., 1995).

The Nd isotope composition of the first group of lamprophyres is consistent with that of Triassic alkaline dyke swarms from the Ivrea-Verbano Zone (Fig. 8) attributed to the transition from post-collisional orogenic to anorogenic alkaline magmatism in the Southern Alps (Ogunyele et al., 2024; Stähle et al., 2001). This might suggests that the first group of lamprophyres share the same mantle source of these

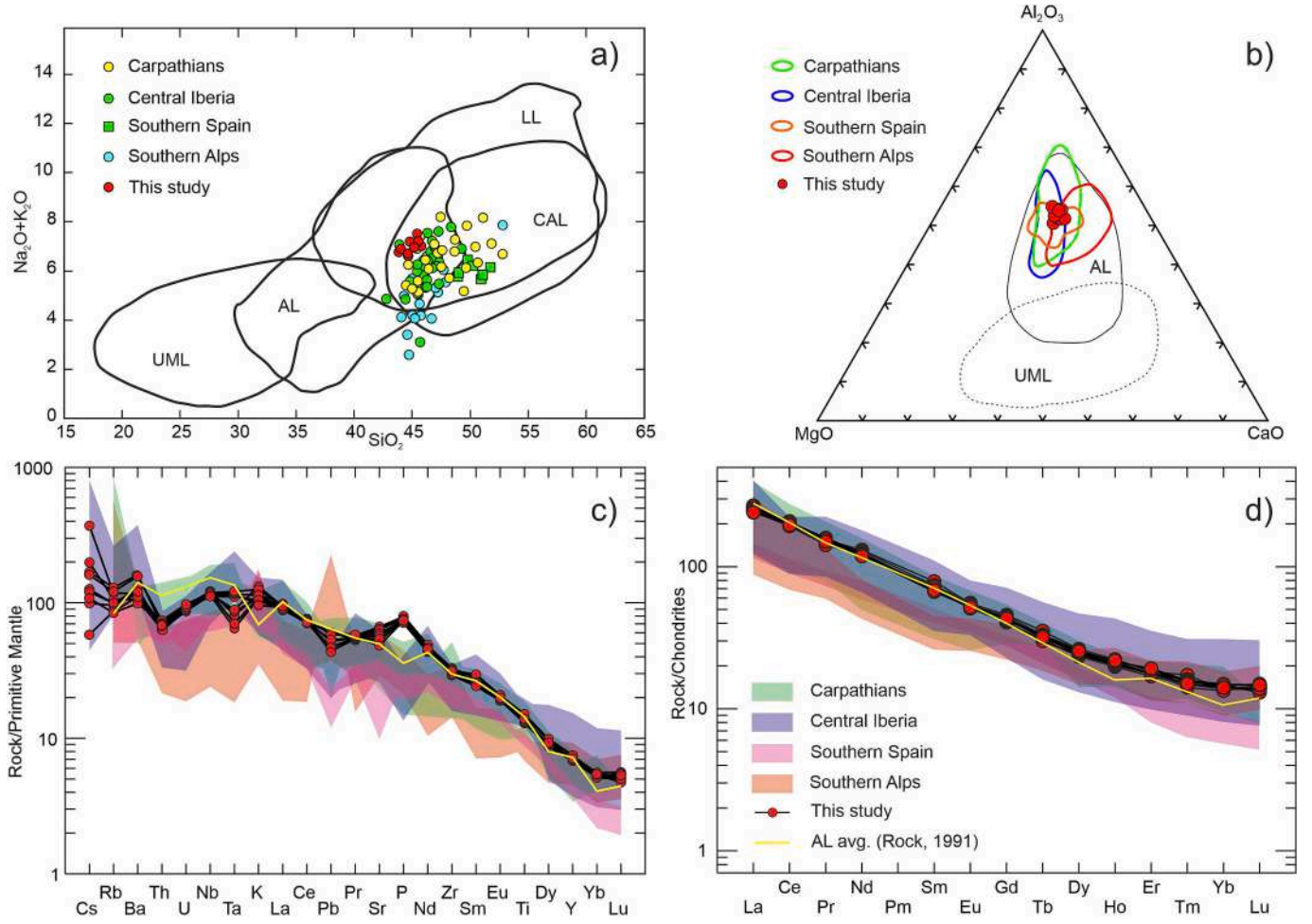

Fig. 7. (a) SiO_2 vs. $Na_2O + K_2O$ wt% and (b) Al_2O_3–MgO–CaO diagrams (Rock, 1987) showing the composition of the studied lamprophyre compared with those of worldwide alkaline lamprophyres (AL), ultramafic lamprophyres (UML), calc-alkaline lamprophyres (CAL), and lamproites (LL); (c) Primitive mantle-normalized (McDonough and Sun, 1995) trace element patterns and (d) Chondrite-normalized REE patterns of the Sardinia FMN lamprophyre. The composition of lamprophyres from Carpathians, Romania (Ditrău Complex, Batki et al., 2014), Central Iberia (Orejana et al., 2008; Scarrow et al., 2011), Southern Spain (Puga et al., 2010), and Southern Alps (Casetta et al., 2019; De Min et al., 2020) are shown for comparison.

Table 4
Radiogenic isotope compositions of selected samples of the lamprophyre dyke. Initial isotopic compositions were calculated at 220 Ma. A 4 % uncertainty in $^{87}Rb/^{86}Sr$ has been determined on the basis of replicate analyses of the samples; uncertainties in measured (m) and initial (i) isotopic compositions refer to the least significant digits and represent $2\sigma_m$ run precision and $2\sigma_m$ error propagation, respectively.

Sample	$^{87}Rb/^{86}Sr$	$^{87}Sr/^{86}Sr_m$	$2\ \sigma_m$	$87Sr/86Sr_i$	$2\ \sigma_m$	$^{147}Sm/^{144}Nd$	$^{143}Nd/^{144}Nd_m$	$2\ \sigma_m$	$143Nd/144Nd_i$	$2\ \sigma_m$
FZ 1	0.1828	0.704698	± 5	0.704126	± 25	0.1213	0.512839	± 6	0.512665	± 9
FZ 2	0.2351	0.704928	± 5	0.704192	± 32	0.1219	0.512839	± 6	0.512664	± 9
FZ 4	0.1667	0.704264	± 6	0.703743	± 23	0.1247	0.512842	± 5	0.512662	± 9
FZ 8	0.1712	0.703959	± 6	0.703423	± 23	0.1206	0.512847	± 6	0.512673	± 9
FZ 11	0.1933	0.704120	± 6	0.703515	± 26	0.1289	0.512805	± 6	0.512620	± 10

alkaline dyke swarms, related to asthenosphere upwelling in an intraplate geodynamic setting and representing a precursor to the rifting stage associated with the opening of the Tethys in the western Mediterranean region (Bonazzi et al., 2020; Casetta et al., 2019; De Min et al., 2020; Galli et al., 2019; Giovanardi et al., 2020; Mazzucchelli et al., 2010; Schaltegger et al., 2015; Stähle et al., 2001).

The second group of lamprophyres has a Sr—Nd isotope composition intermediate between the first group of lamprophyres and the metasomatized subcontinental lithospheric mantle (Fig. 8), suggesting the contribution of both mantle sources to their genesis. This can find a rationale on the basis of radiometric datings: the Central Iberia and the sample from Southern Alps emplaced at 265 Ma and 235 Ma, respectively, whereas the first group of lamprophyres emplaced at 220–200 Ma (De Min et al., 2020). This age difference is consistent with the transition (at least in Southern Alps because in Central Iberia there is no dating of this transition) from Early Mesozoic high-K calcalkaline to shoshonitic post-collisional magmatism originating in the metasomatized subcontinental lithospheric mantle to alkaline anorogenic magmatism originating in the asthenosphere (Casetta et al., 2019, 2021; Cassinis et al., 2008; De Min et al., 2020; Ogunyele et al., 2024). In this scenario the second group of lamprophyres could reflect a mixed contribution of both mantle domains (Fig. 8), being still influenced by the post-collisional settings. Instead, in the younger lamprophyres, the post-collisional signature disappears, showing the affinity related to the later anorogenic phase.

Trace elements provide further constraints on the genesis of these

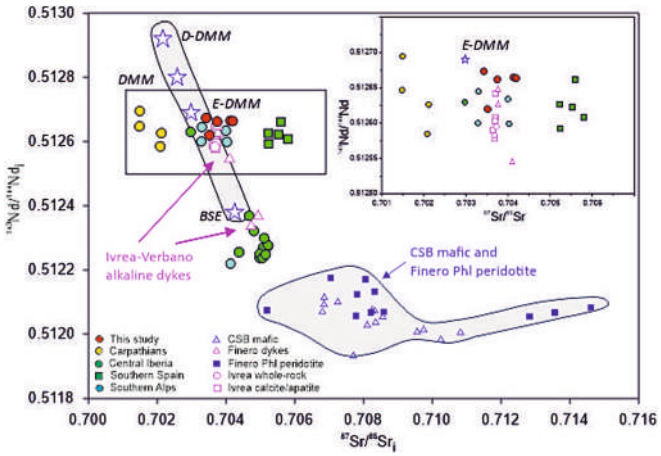

Fig. 8. $^{87}Sr/^{86}Sr_i$ vs. $^{143}Nd/^{144}Nd_i$ diagram showing the initial (220 Ma) isotopic signature of the FMN lamprophyre. The initial Sr—Nd isotopic signature of lamprophyres from Predazzo (Southern Alps, Casetta et al., 2019), Ditrău Complex, Carpathians (Batki et al., 2014), Central Iberia (Orejana et al., 2008) and Southern Spain (Puga et al., 2010) are also shown, together with the depleted MORB mantle (DMM), D-DMM, *E*-DMM mantle sources at 220 Ma (Workman and Hart, 2005) and Bulk Silicate Earth (BSE) of McDonough and Sun (1995). CSB: Corsica-Sardinia Batholith data from Voshage et al. (1987), Tommasini et al. (1995), Franciosi et al. (2019), Secchi et al. (2022).

Table 5
P, T, and H_2O in the melt of the FMN lamprophyre based upon the algorithm of Ridolfi (2021) on single amphibole minerals.

	T(°C)	Err.	P(MPa)	Err.	H_2O(wt%)	Err.
FZ7						
Core	1026–1032	±22	1067–1099	±132	3.9–4.1	±0.7
Rim	1039–1072	±22	500–767	±92	2.7–5.2	±0.9
Groundmass	1059–1065	±22	558–564	±68	3.6–4.2	±0.7
FZ4						
Core	1029	±22	1139	±137	4.1	±0.7
Rim	1064	±22	533	±64	3.8	±0.6
Groundmass	995–1009	±22	500–510	±61	4.0–4.1	±0.7
FZ11						
Core	991–1025	±22	962–1244	±149	4.0–4.3	±0.7
Rim	1054–1057	±22	854–913	±110	3.3	±0.6
Groundmass	1013–1056	±22	695–760	±91	4.1–5.0	±0.9

lamprophyres and their astenospheric source. The REE fractionation in chondrite-normalized patterns (Fig. 7d) suggests derivation from a garnet-lherzolite mantle where residual garnet tends to fractionate HREE ($Gd_n/Yb_n > 2$ in the FMN lamprophyre) whereas the more incompatible LREE are concentrated in the melt. The high Sr/Y values of the Sardinian lamprophyre (~33–42, Table 3) confirm the involvement of garnet as residual phase during mantle melting (Moyen, 2009). The absence of Eu anomalies indicates that plagioclase fractionation —which would produce a negative anomaly— did not occur during magma crystallization.

The lower Zr/Nb and higher La/Yb of the European lamprophyres, compared with Ocean Island Basalts and Mid-Ocean Ridge Basalts (OIB, MORB, Fig. 9a), suggest the involvement of an OIB-like mantle source and a progressive decrease in melting degree (e.g., <5 %, Casetta et al., 2019) of this garnet lherzolite from Southern Alps to Spain and Romania.

Another interesting signature of the two groups of European lamprophyres is reported in Fig. 9b. The first group of lamprophyres, in addition to relatively high Nd isotopes, has Ba/Ce close to the average composition of OIB (Ba/Ce = 4.4 ± 2, 1sd, Halliday et al., 1995) and different from Ba/Ce of MORB (Ba/Ce = 2.9 ± 1.6, 1sd), further suggesting an upwelling mantle source similar to that of OIB-like basalts with minor, if any, contribution of MORB-like mantle (i.e., Depleted Morb Mantle). Overall, these trace element characteristics (Fig. 9) are consistent with the radiogenic isotope signature (Fig. 8), indicating an intraplate geodynamic setting, precursor of the rifting stage connected to the opening of the Tethys Ocean in the western Mediterranean region.

The second group of lamprophyres has unradiogenic Nd isotope composition coupled with Ba/Ce > 10. This signature, akin the Sr—Nd isotope signature, is characteristic of a mantle source region intermediate between that of the first group of lamprophyres and the subcontinental lithospheric mantle metasomatized by subducted sediments (i.e., Ba/Ce > 10, average continental crust) during the Variscan orogenic cycle.

Overall, trace element (Figs. 7, 9) and radiogenic isotopes (Fig. 8) from FMN and other European lamprophyres, suggest a mantle source similar to that of OIB-like basalts, although within an intracontinental geodynamic setting. The data also support a progressive transition between the post-collisional orogenic magmatism to anorogenic rift-related alkaline magmatism during Early Mesozoic break-up of Pangea and opening of the Tethys Ocean.

7.3. *Geodynamic implications*

The geochemical signature of the FMN lamprophyre demonstrates an origin from an asthenospheric garnet-lherzolite mantle source at low

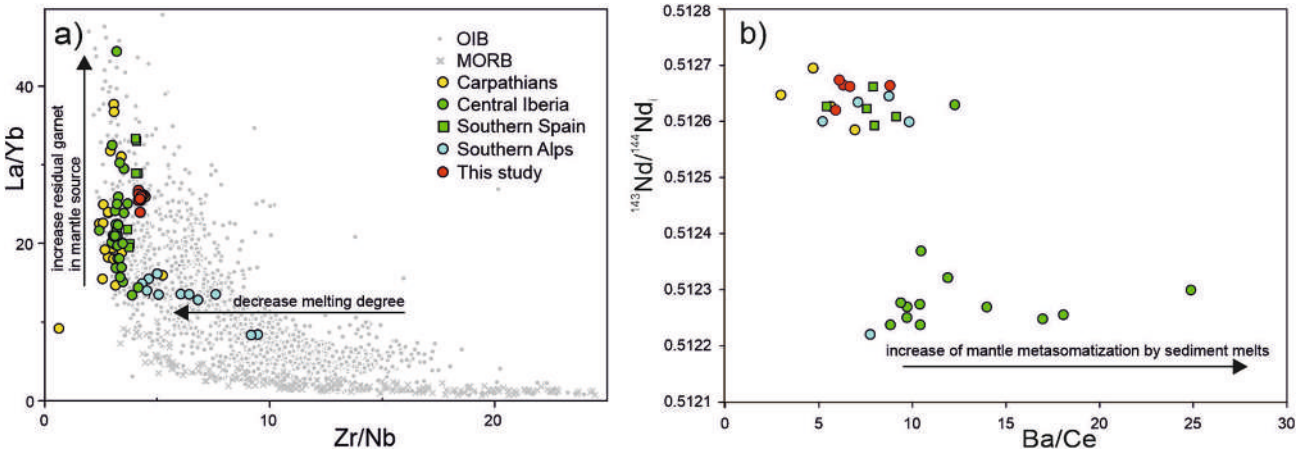

Fig. 9. (a) La/Yb vs. Zr/Nb diagram showing a comparison between the studied samples with other Permian-Triassic lamprophyres from different European regions. The compositions of MORBs and OIBs is also reported for comparison. (b) Ba/Ce vs. Nd isotopic composition of the same samples shown in (a).

melting degrees. The related tectonic scenario reflects an intraplate geodynamic setting that was followed by a rifting stage, with emplacement of the lamprophyre. It is important to compare the new data acquired in this work with those of other European Permo-Triassic lamprophyres of similar age and well constrained tectonic setting (Figs. 7, 8, 9).

In addition to the above-mentioned lamprophyres, Krmíček et al. (2020) described two associations of mantle-derived magmatic rocks in the Bohemian Massif: a lamprophyre-lamproite orogenic association (340–310 Ma) and a lamprophyre association of anorogenic affinity (300–275 Ma). The calc-alkaline lamprophyres occur throughout the entire Saxo-Thuringian and Moldanubian zones, whereas the mantle-derived anorogenic lamprophyres are restricted to the eastern part of the Massif. The Permo-Carboniferous calc-alkaline to alkaline lamprophyres of the Bohemian Massif appear to some extent as a precursor of the geodynamic setting of the Corsica-Sardinia block, although they are older (youngest generation ~275 Ma) and located far in the paleogeographic reconstructions since the Early Permian (Corsini and Rolland, 2009).

The idea that the Pangea started to break-up in early Triassic and that it was accompanied by a widespread magmatism, whose remains are now scattered across central-southern Europe, has reached a wide consensus (Batki et al., 2014; Casetta et al., 2019; De Min et al., 2020 and references therein). Several papers since the 80ies (e.g., Crisci et al., 1984; Pamić, 1984; Pe-Piper, 1998) support this reconstruction based on the evidence provided by structural, geochemical, and geochronological data on different kinds of Triassic magmatic rocks. Indeed, not only alkaline lamprophyres but also shoshonitic/alkaline basalts and andesites, basanites, gabbroic bodies, and carbonatitic melts have been related to the Pangea opening (Batki et al., 2014; De Min et al., 2020; Karsli et al., 2014). For the sake of clarity, all these magmatic rocks that in the literature are referred to the Triassic Pangea break-up will be hereafter referred to as "rifting-related". The geodynamic interpretation of this Triassic magmatism varies from one place to another (from extensional to compressive to transtensional) leading to different hypotheses on their formation (anorogenic rifting, backarc development, subduction setting, etc.) (e.g., Casetta et al., 2019 for updated references) but the final outcome of these movements is in any case the Pangea break-up.

A detailed discussion of the plate motion during the Triassic is beyond the scope of this study but it is interesting to place the "rifting-related" magmatic rocks in their palaeo-positions to understand if they are consistent with palaeogeographic models. De Min et al. (2020) presented a possible scenario of the Pangea opening (based on Schettino and Turco, 2011) in which the alignment of European lamprophyres marks the possible rifting zone; in this framework, Sardinia was located north-west of the Adria Plate. Similarly, Stampfli (2005) placed Sardinia to the north of the Adria Plate. More recently, Scotese and Schettino (2017) proposed a reconstruction where Sardinia is located north to Apulia Plate and west to the Italo-Dinaride block. One of the most recent and complete models of the evolution of the Mediterranean area, from middle Triassic to the present, has been proposed by van Hinsbergen et al. (2020). The palaeogeographic setting of the Mediterranean area during Ladinian (240 Ma) is shown in Fig. 10 (modified after van Hinsbergen et al., 2020), and the position of magmatic rocks that have been interpreted as related to the rifting events are also reported. Several considerations, from both spatial and time-related points of view, arise from the proposed model. The magmatic events, variably correlated to the Pangea break-up, mainly span a temporal range from 230 to 210 Ma. The Iberian Peninsula, is an exception in this framework since its magmatism, mainly consisting of lamprophyres, bostonites and tholeiitic dykes outcropping in Central Iberia, began earlier, since the middle Permian (265 Ma). Different scenarios have been invoked for such a prolonged magmatism, including (i) mantle plume predating the Atlantic opening, (ii) upwelling of hot asthenosphere, (iii) a change from compressive to transtensional regime, (iv) melting of metasomatized lithospheric mantle due to late Variscan extension and decompression (Orejana et al., 2006, 2008; Scarrow et al., 2011; Villaseca et al., 2004). In any case, most of the Iberian "rift-related" magmatism can hardly be used to interpret the geodynamic setting at the European scale, due to its age, duration, and geochemical variability that has been interpreted as the result of several processes. At the best of our knowledge, the only

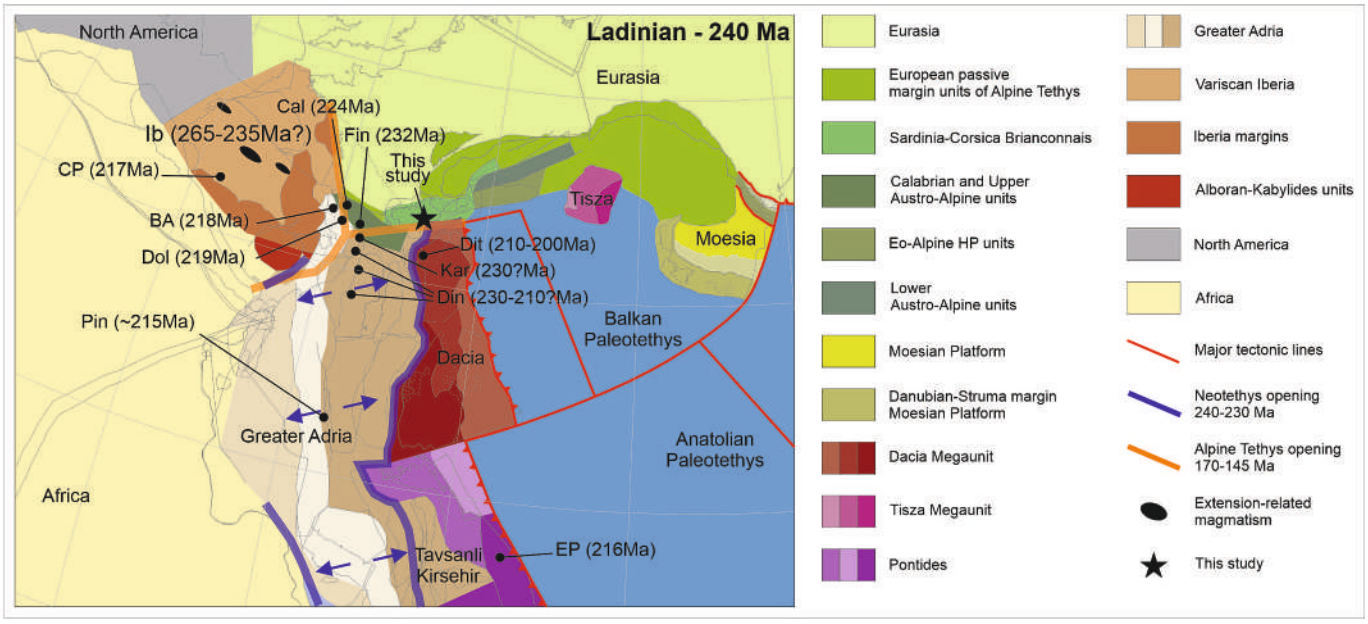

Fig. 10. Palaeotectonic map of the Mediterranean region during the Ladinian (240 Ma) (modified after van Hinsbergen et al., 2020). The position and the age of magmatic rocks that have been related to the Pangea break-up are reported (black dots) together with the traces of Neotethys and Alpine Tethys opening. Ib = Iberian (Orejana et al., 2008; Scarrow et al., 2011; Villaseca et al., 2004); CP=Cerro Prieto (Puga et al., 2010); BA = Brescian Alps (Cassinis et al., 2008); Cal = Calabria (Liberi et al., 2011); Dol = Dolomites (Casetta et al., 2019); Fin = Finero (Zanetti et al., 2013); Dit = Ditrău Complex (Batki et al., 2014; Morogan et al., 2000); Kar = Karawanken (Lippolt and Pidgeon, 1974); Pin = Pindos Nappe (Pe-Piper, 1998); Din = Dinarides (Pamić, 1984; Zelić et al., 2005); EP=Western Pontides (Karsli et al., 2014).

occurrence of alkaline lamprophyres of Triassic age (217 Ma) in Iberia emerged from drill cores in the Sub-Betic Cordillera (Puga et al., 2010).

The spatial distribution of the European Triassic magmatism, restored to its pre-breakup position, is mainly concentrated around the triple point marking the opening of the Alpine Tethys (thick orange lines in Fig. 10). This is the case of the Alpine outcrops of Finero (Ivrea-Verbano Zone, Zanetti et al., 2013), Brescian Alps (Cassinis et al., 2008), Predazzo (Dolomites, Casetta et al., 2019), and also Calabria (Southern Italy, Liberi et al., 2011) and Karawanken complex (Austria, Lippolt and Pidgeon, 1974). The Dinaric magmatism, now spreading from Slovenia to Greece (Monjoie et al., 2008; Pamić, 1984; Pe-Piper, 1998; Zelić et al., 2005), during Triassic followed a south-directed trend along the Adria Plate and sub-parallel (but shifted towards west) to the opening of Neotethys Ocean (blue line in Fig. 10). The easternmost occurrence of rifting-related magmatic rocks is represented by the alkaline lamprophyres of the Ditrău Complex (north-western Carpathians, Romania, Morogan et al., 2000; Batki et al., 2014) and by the calcalkaline lamprophyres in eastern Pontides (Turkey, Karsli et al., 2014), located on the eastern side of Neotethys opening. The Sardinian lamprophyre presented in this study is located along the eastern branch of the fault system that led to the opening of the Alpine Tethys.

The timing and position of the European lamprophyres roughly follow the break-up traces but are not totally in agreement with them. In particular, the Alpine and Calabrian lamprophyres lie quite close to the fault system that led to the Alpine Tethys opening, but their age (220–230 Ma) is significantly older than the presumed age of this opening, which should have started at about 180–170 Ma (van Hinsbergen et al., 2020). Another discrepancy is related to the Triassic location of "rifting related" magmatic rocks of Dinaric and Hellenic domains. Indeed, if compared with the trace of Neotethys opening, they are significantly shifted towards west falling in the middle of the Greater Adria plate. On the other hand, it must be considered that the whole Adria Plate underwent a marked east-west extension (van Hinsbergen et al., 2020) which can explain the widespread alkaline magmatism during middle to late Triassic.

8. Conclusions

The FMN lamprophyre is compositionally similar to other European Permian-Triassic lamprophyres from various European regions.

The amphibole composition of the Sardinian lamprophyre is similar to those reported for several European lamprophyres, from Southern Alps, Ditrău Alkaline massif in Romania, and Central Iberia. In the FMN lamprophyre, the more evolved composition of the wide, homogeneous, Fe-rich/Mg-poor cores of the amphibole macrocrystals indicate that these amphibole domains are antecrysts that crystallized from a relatively evolved magma of deep crustal origin. The cores of these amphiboles were in disequilibrium with the melt, whereas the rim would represent a late overgrowth approaching equilibrium.

The REE systematics and fractionation in chondrite-normalized patterns suggest that the FMN lamprophyre derived from a garnet-lherzolite mantle where residual garnet fractionated HREE. The REE fractionation of Sardinia and other European lamprophyres is consistent with low melting degrees of a primitive mantle source, which experienced melting mainly in the garnet stability field (>70 km depth), similar to most OIBs.

The radiogenic isotope composition of the Sardinian lamprophyre clusters between the *E*-DMM and BSE mantle components at 220 Ma. The radiogenic isotope composition resembles those of OIB-like basalts although emplaced in intracontinental geodynamic settings.

The Sardinian lamprophyre belongs to the wide Triassic, "rifting-related" magmatism which records the Pangea break-up. These rocks are located along the eastern branch of the fault system that led to the opening of the Alpine Tethys, tapping an asthenospheric source with no sign of lithospheric contribution, which is instead recorded in older lamprophyres from Central Iberia and one sample from Southern Alps.

CRediT authorship contribution statement

Gabriele Cruciani: Writing – review & editing, Writing – original draft, Conceptualization, Funding acquisition. **Dario Fancello:** Writing – original draft, Data curation. **Mattia Ferrari:** Formal analysis, Data curation. **Alessandro Bragagni:** Writing – original draft, Formal analysis, Data curation. **Simone Tommasini:** Writing – review & editing, Writing – original draft, Conceptualization. **Marcello Franceschelli:** Writing – review & editing, Writing – original draft, Funding acquisition, Conceptualization.

Funding

Financial support was provided by the research project "Sustainable land management: the tools of geology for the environment" funded by Fondazione di Sardegna CUP F75F21001270007.

Declaration of competing interest

The authors declared that we have no conflicts of interest to this work. We declare that we do not have any commercial or associative interest that represents a conflict of interest in connection with the work submitted.

Acknowledgements

Thomas Theye (Stuttgart) is acknowledged for support during electron microprobe analyses. The authors wish to thank Lukáš Krmíček (Czech Academy of Sciences) and an anonymous reviewer for their helpful comments and constructive criticism.

Appendix A. Supplementary data

Supplementary data to this article can be found online at https://doi.org/10.1016/j.lithos.2025.108106.

References

Adam, J., Green, T.H., 1994. The effects of pressure and temperature on the partitioning of Ti, Sr and REE between amphibole, clinopyroxene and basanitic melts. Chem. Geol. 117 (1–4), 219–233.

Alvarez, W., 1972. Rotation of the Corsica-Sardinia microplate. Nature 235, 103–105.

Avanzinelli, R., Boari, E., Conticelli, S., Francalanci, L., Guarnieri, L., Perini, G., Petrone, M.C., Tommasini, S., Ulivi, M., 2005. High precision Sr, Nd and Pb isotopic analyses using the new generation thermal ionisation mass spectrometer ThermoFinnigan Triton-Ti®. Per. Mineral. 74 (3), 147–166.

Baldelli, C., Bigazzi, G., Elter, F.M., Macera, P., 1987. Description of a permo-trias alkaline lamprophyre embedded into the micaschists of garnet-staurolite-kyanite grade of North-eastern Sardinia island. In: Sassi, F.P., Bourrouilh, R. (Eds.), IGCP n°5 Newsletter 7, pp. 7–10.

Batki, A., Pál-Molnár, E., Dobosi, G., Skelton, A., 2014. Petrogenetic significance of ocellar camptonite dykes in the Ditrău Alkaline Massif, Romania. Lithos 200-201, 181–196.

Bédard, J.H., 1994. Mesozoic east North American alkaline magmatism: part 1. Evolution of Monteregian lamprophyres, Québec, Canada. Geochim. Cosmochim. Acta 58, 95–112.

Bergman, S.C., 1987. Lamproites and other potassium-rich igneous rocks: a review of their occurrence, mineralogy and geochemistry. Geol. Soc. London, Special Publ. 30, 103–190. https://doi.org/10.1144/GSL.SP.1987.030.01.08.

Bernard-Griffiths, J., Fourcade, S., Dupuy, C., 1991. Isotopic study (Sr, Nd, O and C) of lamprophyres and associated dykes from Tamazert (Morocco): crustal contamination processes and source characteristics. Earth Planet. Sci. Lett. 103, 190–199.

Bonazzi, M., Langone, A., Tumiati, S., Dellarole, E., Mazzucchelli, M., Giovanardi, T., Zanetti, A., 2020. Mantle-derived corundum-bearing felsic dykes may survive only within the lower (refractory/inert) crust: evidence from zircon geochemistry and geochronology (Ivrea–Verbano zone, Southern Alps, Italy). Geosciences 10 (8), 281. https://doi.org/10.3390/geosciences10080281.

Bouabdli, A., Dupuy, C., Dostal, J., 1988. Geochemistry of Mesozoic alkaline lamprophyres and related rocks from the Tamazert massif, High Atlas (Morocco). Lithos 22, 43–58.

Carmignani, L., Oggiano, G., Barca, S., Conti, P., Eltrudis, A., Funedda, A., Pasci, S., Salvadori, I., 2001. Geologia della Sardegna (Note illustrative della Carta Geologica della Sardegna in scala 1:200000). In: Mem. Descr. Carta Geol. It., Vol. LX. Servizio Geologico Nazionale. Istituto Poligrafico e Zecca dello Stato, Roma, 283 pp.

Carosi, R., Petroccia, A., Iaccarino, S., Simonetti, M., Langone, A., Montomoli, C., 2020. Kinematics and timing constraints in a transpressive tectonic regime: the example of the Posada-Asinara Shear Zone (NE Sardinia, Italy). Geosciences 10, 288.

Casetta, F., Ickert, R.B., Mark, D.F., Bonadiman, C., Giacomoni, P.P., Ntaflos, T., Coltorti, M., 2019. The alkaline lamprophyres of the Dolomitic area (Southern Alps, Italy): markers of the Late Triassic change from orogenic-like to anorogenic magmatism. J. Petrol. 60, 1263–1298.

Casetta, F., Ickert, R.B., Mark, D.F., Giacomoni, P.P., Bonadiman, C., Ntaflos, T., Zanetti, A., Coltorti, M., 2021. The Variscan subduction inheritance in the Southern Alps Sub-Continental Lithospheric Mantle: Clues from the Middle Triassic shoshonitic magmatism of the Dolomites (NE Italy). Lithos 380–381, 105856. https://doi.org/10.1016/j.lithos.2020.105856.

Casini, L., Cuccuru, S., Maino, M., Oggiano, G., Tiepolo, M., 2012. Emplacement of the Arzachena pluton (Corsica-Sardinia batholith) and the geodynamics of the incoming Pangea. Tectonophysics 544–545, 31–49.

Cassinis, G., Cortesogno, L., Gaggero, L., Perotti, C.R., Buzzi, L., 2008. Permian to Triassic geodynamic and magmatic evolution of the Brescian Prealps (eastern Lombardy, Italy). Boll. Soc. Geol. Italy 127, 501–518.

Castellarin, A., Lucchini, F., Rossi, P.L., Selli, L., Simboli, G., 1988. The Middle Triassic magmatic–tectonic arc development in the Southern Alps. Tectonophysics 146, 79–89.

Corsini, M., Rolland, Y., 2009. Late evolution of the southern European Variscan belt: exhumation of the lower crust in a context of oblique convergence. C.R. Geosci. 341, 214–223.

Cortesogno, L., Cassinis, G., Dallagiovanna, G., Gaggero, L., Oggiano, G., Ronchi, A., Seno, S., Vanossi, M., 1998. The Variscan post-collisional volcanism in Late Carboniferous-Permian sequences of Ligurian Alps, Southern Alps and Sardinia (Italy): a synthesis. Lithos 45, 305–328.

Crisci, C.M., Ferrara, G., Mazzuoli, R., Rossi, P.M., 1984. Geochemical and geochronological data on Triassic volcanism of the Southern Alps of Lombardy (Italy): genetic implications. Geol. Rundsch. 73 (1), 279–292.

Cruciani, G., Montomoli, C., Carosi, R., Franceschelli, M., Puxeddu, M., 2015. Continental collision from two perspectives: a review of Variscan metamorphism and deformation in northern Sardinia. Per. Mineral. 84, 657–699.

Cruciani, G., Franceschelli, M., Massonne, H.-J., Musumeci, G., 2021. Evidence of two metamorphic cycles preserved in garnet from felsic granulite in the southern Variscan belt of Corsica, France. Lithos 380–381, 105919.

Cruciani, G., Franceschelli, M., Carosi, R., Montomoli, C., 2022. P-T path from garnet zoning in pelitic schist from NE Sardinia, Italy: further constraints on the metamorphic and tectonic evolution of the North Sardinia Variscan belt. Lithos 428–429, 106836.

De Min, A., Velicogna, M., Ziberna, L., Chiaradia, M., Alberti, A., Marzoli, A., 2020. Triassic magmatism in the European Southern Alps as an early phase of Pangea break-up. Geol. Mag. 157 (11), 1800–1822.

Fancello, D., Cruciani, G., Franceschelli, M., Massonne, H.-J., 2018. Trondhjemitic leucosomes in paragneisses from NE Sardinia: geochemistry and P-T conditions of melting and crystallization. Lithos 304–307, 501–517.

Franciosi, L., D'Antonio, M., Fedele, L., Guarino, V., Tassinari, C.C.G., de Gennaro, R., Cucciniello, C., 2019. Petrogenesis of the Solanas gabbro-granodiorite intrusion, Sarrabus (southeastern Sardinia, Italy): implications for late Variscan magmatism. Int. J. Earth Sci. 108, 989–1012.

Gaggero, L., Oggiano, G., Buzzi, L., Slejko, F., Cortesogno, F., 2007. Post-Variscan mafic dikes from the late orogenic collapse to the Tethyan rift: evidence from Sardinia. Ofioliti 32, 15–37.

Gaggero, L., Gretter, N., Langone, A., Ronchi, A., 2017. U–Pb geochronology and geochemistry of late Palaeozoic volcanism in Sardinia (southern Variscides). Geosci. Front. 8, 1263–1284.

Galli, A., Grassi, D., Sartori, G., Gianola, O., Burg, J.-P., Schmidt, M.W., 2019. Jurassic carbonatite and alkaline magmatism in the Ivrea zone (European Alps) related to the breakup of Pangea. Geology 47, 199–202.

Giovanardi, T., Zanetti, A., Dallai, L., Morishita, T., Hémond, C., Mazzucchelli, M., 2020. Evidence of subduction-related components in sapphirine-bearing gabbroic dykes (Finero phlogopite–peridotite): insights into the source of the Triassic-Jurassic magmatism at the Europe-Africa boundary. Lithos 356–357, 105366. https://doi.org/10.1016/j.lithos.2020.105366.

Halliday, A.N., Lee, D.-C., Tommasini, S., Davies, G.R., Paslick, C.R., Fitton, J.G., James, D.E., 1995. Incompatible trace elements in OIB and MORB and source enrichment in the sub-oceanic mantle. Earth Planet. Sci. Lett. 133, 379–395.

Hawthorne, F.C., Oberti, R., Harlow, G.E., Maresch, W.V., Martin, R.F., Schumacher, J. C., Welch, M.D., 2012. IMA report—nomenclature of the amphibole supergroup. Am. Mineral. 97, 2031–2048.

Hidas, K., Guzmics, T., Szabó, C., Kovács, I., Bodnar, R.J., Zajacz, Z., Nédli, Z., Vaccari, L., Perucchi, A., 2010. Coexisting silicate melt inclusions and H_2O-bearing, CO_2-rich fluid inclusions in mantle peridotite xenoliths from the Carpathian–Pannonian region (central Hungary). Chem. Geol. 274, 1–18.

Karsli, O., Dokuz, A., Kaliwoda, M., Uysal, I., Aydin, F., Kandemir, R., Fehr, K.T., 2014. Geochemical fingerprints of Late Triassic calc-alkaline lamprophyres from the Eastern Pontides, NE Turkey: a key to understanding lamprophyre formation in a subduction-related environment. Lithos 196, 181–197.

Krmíček, L., Chalapathi Rao, N.V., 2021. Lamprophyres, lamproites and related rocks: tracers to supercontinent cycles and metallogenesis. Geol. Soc. Lond. Spec. Publ. 513, 1–16.

Krmíček, L., Cempírek, J., Havlín, A., Přichystal, A., Houzar, S., Krmíčková, M., Gadas, P., 2011. Mineralogy and petrogenesis of a Ba–Ti–Zr-rich peralkaline dyke from Šebkovice (Czech Republic): recognition of the most lamproitic Variscan intrusion. Lithos 121, 74–86.

Krmíček, L., Romer, R.L., Timmerman, M.J., Ulrych, J., Glodny, J., Přichystal, A., Sudo, M., 2020. Long-lasting (65 Ma) regionally contrasting late- to post-orogenic Variscan mantle-derived potassic magmatism in the Bohemian Massif. J. Petrol. 61 (7), egaa072. https://doi.org/10.1093/petrology/egaa072.

Lang, M., Zhang, Z., Chen, Z., Cheng, Z., Santosh, M., Kusky, T.M., 2023. Classification and nomenclature of volcanic rocks using immobile elements: a novel approach based on big data analysis. Lithos 454-455, 107274.

Li, X., Zhang, C., Behrens, H., Holtz, F., 2020. Calculating biotite formula from electron microprobe analysis data using a machine learning method based on principal components regression. Lithos 356–357, 105371.

Liberi, F., Piluso, E., Langone, A., 2011. Permo-Triassic thermal events in the lower Variscan continental crust section of the Northern Calabrian Arc, Southern Italy: insights from petrological data and in situ U–Pb zircon geochronology on gabbros. Lithos 124, 291–307.

Lippolt, H.J., Pidgeon, R., 1974. Isotopic mineral ages of a diorite from the Eisenkappel intrusion, Austria. Zeitschrift für Naturforschung A 29 (6), 966–968.

Liu, B.X., Zhang, Z.C., Giuliani, A., Xie, Q.H., Kong, W.L., Wang, C., Wei, B.W., Ke, S., Santosh, M., Zhang, B., Zhang, X.C., Krmíček, L., 2023. A mantle plume connection for alkaline lamprophyres (sannaites) from the Permian Tarim Large Igneous Province: petrological, geochemical and isotopic constraints. J. Petrol. 64 (2), egad004. https://doi.org/10.1093/petrology/egad004.

Locock, A.J., 2014. An Excel spreadsheet to classify chemical analyses of amphiboles following the IMA 2012 recommendations. Comput. Geosci. 62, 1–11.

Lu, Y.J., McCuaig, T.C., Li, Z.X., Jourdan, F., Hart, C.J., Hou, Z.Q., Tang, S.H., 2015. Paleogene post-collisional lamprophyres in western Yunnan, western Yangtze Craton: mantle source and tectonic implications. Lithos 233, 139–161.

Mazzucchelli, M., Zanetti, A., Rivalenti, G., Vannucci, R., Correia, C.T., Tassinari, C.C.G., 2010. Age and geochemistry of mantle peridotites and diorite dykes from the Baldissero body: insights into the Paleozoic-Mesozoic evolution of the Southern Alps. Lithos 119, 485–500.

McDonough, W.F., Sun, S.S., 1995. The composition of the Earth. Chem. Geol. 120, 223–253.

Monjoie, P., Lapierre, H., Tashko, A., Mascle, G.H., Dechamp, A., Muceku, B., Brunet, P., 2008. Nature and origin of the Triassic volcanism in Albania and Othrys: a key to understanding the Neotethys opening? Bull. Soc. Géol. France 179 (4), 411–425.

Morogan, V., Upton, B.G.J., Fitton, J.G., 2000. The petrology of the Ditrau alkaline complex, Eastern Carpathians. Mineral. Petrol. 69 (3), 227–265.

Moyen, J.F., 2009. High Sr/Y and La/Yb ratios: the meaning of the "adakitic signature". Lithos 112 (3–4), 556–574.

Ogunyele, A.C., Bonazzi, M., Giovanardi, T., Mazzucchelli, M., Salters, V.J.M., Decarlis, A., Sanfilippo, A., Zanetti, A., 2024. Transition from orogenic-like to anorogenic magmatism in the Southern Alps during the Early Mesozoic: Evidence from elemental and Nd-Sr-Hf Pb isotope geochemistry of alkali-rich dykes from the Finero Phlogopite Peridotite. Ivrea–Verbano Zone. Gondwana Res. 129, 201–219. https://doi.org/10.1016/j.gr.2023.12.011.

Orejana, D., Villaseca, C., Paterson, B.A., 2006. Geochemistry of pyroxenitic and hornblenditic xenoliths in alkaline lamprophyres from the Spanish Central System. Lithos 86 (1–2), 167–196.

Orejana, D., Villaseca, C., Billström, K., Paterson, B.A., 2008. Petrogenesis of Permian alkaline lamprophyres and diabases from the Spanish Central System and their geodynamic context within western Europe. Contrib. Mineral. Petrol. 156 (4), 477–500.

Pamić, J.J., 1984. Triassic magmatism of the Dinarides in Yugoslavia. Tectonophysics 109, 273–307.

Pandey, A., Rao, N.C., Chakrabarti, R., Pandit, D., Pankaj, P., Kumar, A., Sahoo, S., 2017a. Petrogenesis of a Mesoproterozoic shoshonitic lamprophyre dyke from the Wajrakarur kimberlite field, eastern Dharwar craton, southern India: geochemical and Sr–Nd isotopic evidence for a modified sub-continental lithospheric mantle source. Lithos 292, 218–233.

Pandey, A., Rao, N.C., Pandit, D., Pankaj, P., Pandey, R., Sahoo, S., Kumar, A., 2017b. Subduction–tectonics in the evolution of the eastern Dharwar craton, southern India: insights from the post-collisional calc-alkaline lamprophyres at the western margin of the Cuddapah basin. Prec. Res. 298, 235–251.

Pe-Piper, G., 1998. The nature of Triassic extension-related magmatism in Greece: evidence from Nd and Pb isotope geochemistry. Geol. Mag. 135 (3), 331–348.

Pilet, S., Ulmer, P., Villiger, S., 2010. Liquid line of descent of a basanitic liquid at 1.5 GPa: constraints on the formation of metasomatic veins. Contrib. Mineral. Petrol. 159, 621–643.

Puga, E., Beccaluva, L., Bianchini, G., Díaz de Federico, A., Díaz Puga, M.A., Alvarez-Valero, A.M., Galindo-Zaldívar, J., Wijbrans, J.R., 2010. First evidence of lamprophyric magmatism within the Subbetic Zone (Southern Spain). Geol. Acta 8 (2), 111–130.

Putirka, K., 2016. Amphibole thermometers and barometers for igneous systems and some implications for eruption mechanisms of felsic magmas at arc volcanoes. Am. Mineral. 101 (4), 841–858.

Ridolfi, F., 2021. Amp-TB2: an updated model for calcic amphibole thermobarometry. Minerals 11, 324. https://doi.org/10.3390/min11030324.

Rock, N.M.S., 1987. The nature and origin of lamprophyres: an overview. In: Fitton, J.G., Upton, B.G.J. (Eds.), Alkaline Igneous Rocks, Geol. Soc., London, Special Publ, 30, pp. 191–226.

Rock, N.M.S., 1991. Lamprophyres. Van Nostrand Reinhold, Glasgow, London: Blackie; New York, 285 pp.

Rossi, P., Oggiano, G., Cocherie, A., 2009. A restored section of the "southern Variscan realm" across the Corsica–Sardinia microcontinent. C. R. Geosci. 341, 224–238.

Scarrow, J.H., Molina, J.F., Bea, F., Montero, P., Vaughan, A.P., 2011. Lamprophyre dikes as tectonic markers of late orogenic transtension timing and kinematics: a case study from the Central Iberian Zone. Tectonics 30, TC4007.
Schaltegger, U., Ulianov, A., Müntener, O., Ovtcharova, M., Peytcheva, I., Vonlanthen, P., Vennemann, T., Antognini, M., Girlanda, F., 2015. Megacrystic zircon with planar fractures in miaskite-type nepheline pegmatites formed at high pressures in the lower crust (Ivrea Zone, southern Alps, Switzerland). Am. Mineral. 100, 83–94.
Schettino, A., Turco, E., 2011. Tectonic history of the western Tethys since the Late Triassic. Geol. Soc. Am. Bull. 123, 89–105.
Scodina, M., Cruciani, G., Franceschelli, M., Massonne, H.-J., 2019. Anticlockwise P-T evolution of amphibolites from NE Sardinia, Italy: geodynamic implications for the tectonic evolution of the Variscan Corsica-Sardinia block. Lithos 324, 763–775.
Scotese, C.R., Schettino, A., 2017. Late Permian-Early Jurassic paleogeography of western Tethys and the world. In: Permo-Triassic Salt Provinces of Europe, North Africa and the Atlantic Margins. Elsevier, pp. 57–95.
Secchi, F., Giovanardi, T., Naitza, S., Casalini, M., Kohút, M., Conte, A.M., Oggiano, G., 2022. Multiple crustal and mantle inputs in post-collisional magmatism: evidence from late-Variscan Sarrabus pluton (SE Sardinia, Italy). Lithos 420–421, 106697. https://doi.org/10.1016/j.lithos.2022.106697.
Serre, S.H., van der Meer, Q.H., Waight, T.E., Scott, J.M., Muenker, C., Thomsen, T.B., le Roux, P.J., 2020. Petrogenesis of amphibole megacrysts in lamprophyric intraplate magmatism in southern New Zealand. New Zeal. J. Geol. Geop. 63 (4), 489–509.
Shaw, C.S.J., Eyzaguirre, J., 2000. Origin of megacrysts in the mafic alkaline lavas of the West Eifel volcanic field, Germany. Lithos 50, 75–95.
Soder, C.G., Romer, R.L., 2018. Post-collisional potassic–ultrapotassic magmatism of the Variscan orogen: implications for mantle metasomatism during continental subduction. J. Petrol. 59 (6), 1007–1034.
Stähle, V., Frenzel, G., Hess, J.C., Saupé, F., Schmidt, S.T., Schneider, W., 2001. Permian metabasalt and Triassic alkaline dykes in the northern Ivrea zone: clues to the post-Variscan geodynamic evolution of the Southern Alps. Schweiz. Mineral. Petrog. Mitt. 81, 1–21.
Stampfli, G.M., 2005. Plate tectonic of the Apulia-Adria microcontinents. In: Finett, I.R. (Ed.), CROP PROJECT: Deep Seismic Exploration of the Mediterranean and Italy. Elsevier, the Netherlands, pp. 747–766.
Stoppa, F., Rukhlov, A.S., Bell, K., Schiazza, M., Vichi, G., 2014. Lamprophyres of Italy: early Cretaceous alkaline lamprophyres of Southern Tuscany, Italy. Lithos 188, 97–112.
Tappe, S., Folet, S.F., Jenner, G.A., Heaman, L.M., Kjarsgaard, B.A., Romer, R.L., Stracke, A., Joyce, N., Hoefs, J., 2006. Genesis of ultramafic lamprophyres and carbonatites at Aillik Bay, Labrador: a consequence of incipient lithospheric thinning beneath the North Atlantic Craton. J. Petrol. 47, 1261–1315.
Tommasini, S., Poli, G., Halliday, A.N., 1995. The role of sediment subduction and crustal growth in Hercynian plutonism: isotopic and trace element evidence from the Sardinia–Corsica Batholith. J. Petrol. 36, 1305–1332.
Torres García, M.F., Calderón, M., Ramírez de Arellano, C., Hervé, F., Opitz, J., Theye, T., Fanning, C.M., Pankhurst, R.J., González-Guillot, M., Fuentes, F., Babinski, M., 2020. Trace element composition of amphibole and petrogenesis of hornblendites and plutonic suites of Cretaceous magmatic arcs developed in the Fuegian Andes, southernmost South America. Lithos 372-373, 105656.
Traversa, G., Ronca, S., Pasquali, C., 1997. Post-hercynian basic dyke magmatism of the Concas-Alà dei Sardi alignment (Northern Sardinia-Italy). Per. Mineral. 66, 233–262.
Traversa, G., Ronca, S., Del Moro, A., Pasquali, C., Buraglini, N., Barabino, G., 2003. Late to post-Hercynian dike activity in the Sardinia-Corsica Domain: a transition from orogenic calc-alkaline to anorogenic alkaline magmatism. Boll. Soc. Geol. Italy 2, 131–152.
Ubide, T., Galé, C., Arranz, E., Lago, M., Larrea, P., 2014. Clinopyroxene and amphibole crystal populations in a lamprophyre sill from the Catalonian Coastal Ranges (NE Spain): a record of magma history and a window to mineral–melt partitioning. Lithos 184, 225–242.
Vaccaro, C., Atzori, P., Del Moro, A., Oddone, N., Traversa, G., Villa, I.M., 1991. Geochronology and Sr isotope geochemistry of late - Hercynian dikes from Sardinia. Schweiz. Mineral. Petrogr. Mitt. 71, 221–230.
Van Hinsbergen, D.J.J., Torsvik, T.H., Schmid, S.M., Maţenco, L.C., Maffione, M., Vissers, R.L.M., Gürer, D., Spakman, W., 2020. Orogenic architecture of the Mediterranean region and kinematic reconstruction of its tectonic evolution since the Triassic. Gondw. Res. 81, 79–229.
Vichi, G., Stoppa, F., Wall, F., 2005. The carbonate fraction in carbonatitic Italian lamprophyres. Lithos 85, 154–170.
Villaseca, C., Orejana, D., Pin, C., López García, J.A., Andonaegui, P., 2004. Le magmatisme basique hercynien et post-hercynien du Système central espagnol: essai de caractérisation des sources mantelliques. C. R. Geosci. 336 (10), 877–888.
Voshage, H., Hunziker, J.C., Hofmann, A.W., Zingg, A., 1987. A Nd and Sr isotopic study of the Ivrea zone, Southern Alps, N-Italy. Contrib. Mineral. Petrol. 97, 31–42.
Whitney, D.L., Evans, B.W., 2010. Abbreviations for names of rock-forming minerals. Am. Mineral. 95, 185–187.
Winchester, J.A., Floyd, P.A., 1977. Geochemical discrimination of different magma series and their differentiation products using immobile elements. Chem. Geol. 20, 325–343.
Workman, R.K., Hart, S.R., 2005. Major and trace element composition of the depleted MORB mantle (DMM). Earth Planet. Sci. Lett. 231, 53–72.
Zanetti, A., Mazzucchelli, M., Sinigoi, S., Giovanardi, T., Peressini, G., Fanning, M., 2013. SHRIMP U-Pb zircon Triassic intrusion age of the Finero mafic complex (Ivrea-Verbano zone, Western Alps) and its geodynamic implications. J. Petrol. 54, 2235–2265.
Zelić, M., D'Orazio, M., Malasoma, A., Marroni, M., Pandolfi, L., 2005. The metabasites from the Kopaonik metamorphic complex, Vardar Zone, southern Serbia: remnants of the rifting-related magmatism of the mesotethyan domain or evidence for Paleotethys closure in the Dinaric-Hellenic belt? Ofioliti 30 (2), 91–101.